ELSEVIER

Contents lists available at ScienceDirect

Chemical Engineering Journal

journal homepage: www.elsevier.com/locate/cej



Dynamics and mechanisms of flame spray pyrolysis of LiMn₂O₄ nanoparticles: A reactive molecular dynamics study

Yi Wang^a, Muye Feng^b, Dingyu Hou^c, Ruitian He^d, Kai Hong Luo^{a,d,*}

- ^a Center for Combustion Energy, Department of Energy and Power Engineering, Key Laboratory for Thermal Science and Power Engineering of Ministry of Education, Low Carbon Energy and CCUS Research Center, Institute for Carbon Neutrality, Tsinghua University, Beijing 100084, China
- ^b School of Mechanical and Power Engineering, Nanjing Tech University, Nanjing 211816, China
- ^c Beijing National Laboratory for Molecular Sciences, State Key Laboratory of Polymer Physics and Chemistry, Institute of Chemistry, Chinese Academy of Sciences, Beijing 100190. China
- d Department of Mechanical Engineering, University College London, Torrington Place, London WC1E 7JE, UK

ARTICLE INFO

Keywords: Flame spray pyrolysis Cathode Materials Nanoparticles LiMn₂O₄ Molecular dynamics simulation

ABSTRACT

LiMn₂O₄ is a promising cathode material for lithium-ion batteries. In this study, the synthesis of LiMn₂O₄ nanoparticles via flame spray pyrolysis (FSP) is investigated using reactive force-field (ReaxFF) molecular dynamics simulations. The study provides a detailed atomic-level view of the reaction pathways throughout the FSP process, from precursor droplet evaporation to nucleation and the growth mechanisms of nanoparticles. Based on temperature and oxygen content profiles, the FSP process is divided into four distinct stages: evaporation and initial decomposition, combustion-driven oxidation, nucleation, and particle growth through accretion and agglomeration. In an oxidizing atmosphere, precursor evaporation occurs alongside oxidation reactions, with Licontaining precursors decomposing and diffusing more rapidly than Mn-containing precursors due to Li's lower atomic mass and valence. At higher combustion temperatures (T_c), Mn-containing species exhibit temperaturedependent reaction pathways, favoring oxidized intermediates such as MnO2 and MnO2H, whereas Li follows a consistent reaction pathway across different T_c values, with T_c primarily affecting the intermediate concentrations. Nucleation is Mn-dominated, with $Mn_xO_vH_z$ (x, y, z > 0) frameworks forming and merging preferentially at higher Tc, while Li is passively incorporated into Mn clusters or organic fragments. Early-stage clusters grow by molecular accretion before transitioning to agglomeration, where organic bonds facilitate the formation of soft agglomerates. By the end of the FSP process, nanoparticles containing Li and Mn oxides form, serving as precursors for crystallized LiMn₂O₄. Iterative oxidative annealing refines these amorphous nanoparticles into Li/ Mn oxides, which contain local LiMn₂O₄ spinel crystallites, consistent with experimental TEM observations.

1. Introduction

Over the past few decades, significant efforts have been made to address the challenges posed by the fossil fuel usage, particularly the energy sustainability and climate/environment issues. Lithium-ion batteries (LIBs) are a promising technology for power and energy storage that have drawn much attention [1,2]. Currently, LIBs are used in various applications, including portable electronic devices, electric vehicles, energy storage systems, consumer electronics, medical devices, and military equipment [3], facilitating the transition to a low-carbon global energy system.

The performance and durability of LIBs depend critically on the materials and designs of electrodes. Despite substantial advances in

anode materials [4,5], cathode materials continue to be the bottlenecks that hinder cycling stability and energy density [6]. Among the various candidates, LiMn₂O₄ stands out as a promising cathode material due to its acceptable specific energy density, high working voltage, assured safety performance, cost-effectiveness and sustainable prospects [7–9]. The LiMn₂O₄ spinel crystallizes in a cubic structure with space group symmetry Fd3m, where Li and Mn occupy tetrahedral 8a sites and octahedral 16d sites, respectively [10]. The ordered Mn₂O₄ edge-shared hosts construct an open framework channel to allow the diffusion of Li in three dimensions [11]. However, the capacity fading due to Mn dissolution into the electrolyte is a key challenge for LiMn₂O₄ cathode materials [11]. Additionally, bulk LiMn₂O₄ exhibits low diffusion coefficients, which limits its charge/discharge performance [12,13]. To

^{*} Corresponding author at: Department of Mechanical Engineering, University College London, Torrington Place, London WC1E 7JE, UK. E-mail address: k.luo@ucl.ac.uk (K.H. Luo).

overcome these problems, highly crystalline and stoichiometric ${\rm LiMn_2O_4}$ with smaller particle sizes is required [14–16]. Nanoparticles are especially beneficial, as they offer high specific areas, which enhances the contact between the cathode and electrolyte. This increased surface area improves electronic transport and facilitates lithium diffusion by shortening the diffusion path length, ultimately enhancing the charge/discharge rate and reducing diffusion limitations [16–18].

The synthetic route significantly influences the phase, structure, and electrochemical properties of ${\rm LiMn_2O_4}.$ Common methods for cathode production include solid-state, ion-exchange, soft chemical synthesis, and co-precipitation [19]. However, these methods are often complex, time-consuming, and energy-intensive, requiring precise control over reaction environments, which poses challenges for large-scale production and drives up costs. These limitations hinder the ability to meet the growing production demands for LIBs.

In contrast, flame spray pyrolysis (FSP) has emerged as a promising alternative for producing nanomaterials [20]. FSP offers significant advantages over traditional methods, including simplicity, rapid reaction kinetics, scalability, low energy consumption, and the ability to produce materials with high purity, homogeneity, and controlled product morphology [21–23]. Thanks to these benefits, flame synthesis has been successfully applied to produce LIBs cathode materials [24], showing strong potential for future advancements in battery technology.

FSP has been successfully applied to the synthesis of various cathode materials, including LiCoO2 [25], LiFePO4 [26], nickel-rich cathodes [27], and LiMn₂O₄ [17]. In the case of LiMn₂O₄, an aqueous precursor solution has been used to produce nanoparticles with a size distribution ranging from nano- to sub-micron scale, and traces of Mn₃O₄ were detected [28]. This phenomenon has also been observed when using non-aqueous precursor solutions [29]. By controlling combustion enthalpy, LiMn₂O₄ nanoparticles with varying specific surface areas have been successfully synthesized [30]. Additionally, LiMn₂O₄/carbon nanocomposites have been produced by combining a flame spray with a diffusion flame, allowing for variation in carbon content [31]. Nanostructured LiMn₂O₄ thin films have also been fabricated using flame spray deposition with an organic precursor solution [32]. Key parameters such as reaction temperature, precursor type, and subsequent agglomeration have been systematically analyzed during the FSP production of LiMn₂O₄, providing insights into the material's structural evolution for potential optimization of electrochemical performance.

While significant progress towards improving the cathode material performance through FSP has been achieved, the rapid reaction kinetics limit direct experimental observation of intermediate processes, leading most studies to focus primarily on analyzing the final product's structure and properties. This creates a gap in understanding the underlying reaction mechanisms at the atomic scale. To bridge this gap, molecular dynamics (MD) simulations serve as a powerful tool for studying the synthesis of novel materials at the nanoscale [33]. The ReaxFF MD method, which incorporates quantum chemistry information into classical MD, can accurately describe bond formation and breaking, making it ideal for exploring the reaction mechanisms involved in FSP [33]. ReaxFF MD has been successfully applied in various fields, including combustion, catalysis, and materials science [33–37].

FSP in liquid-fed flames involves multiple physicochemical processes [20]. MD simulations have been widely applied to study these processes, such as pyrolysis reaction [38], nucleation [39], coagulation [40], and sintering [41], all of which play a role during FSP. For LIBs materials, ReaxFF MD has been employed to study TiO_2 , a typical anode material. Wei et al. [42] investigated the hydrolysis of TTIP during the early stages of FSP for TiO_2 , while Hou et al. [43] expanded on this by exploring the nucleation mechanisms leading to Ti-containing clusters.

For LiMn₂O₄ cathode materials, Reddivari et al. [44] utilized ReaxFF MD to investigate the reactions occurring at the LiMn₂O₄ cathode-electrolyte interface, providing insights into manganese dissolution mechanisms. Furthermore, Talkhoncheh et al. [45] demonstrated that attaching an ion pair to the LiMn₂O₄ cathode surface facilitates the

formation of a self-healing cathode-electrolyte interface, which could enhance long-term stability. However, to the best of the authors' knowledge, limited research has focused on the reaction mechanisms during the FSP of LiMn $_2$ O $_4$ materials.

In this study, ReaxFF MD is employed to model the formation mechanisms of LiMn $_2$ O $_4$ during FSP, capturing atomistic interactions and reaction pathways across nanometer-to-micrometer particle sizes. By elucidating the reaction mechanisms and structural evolution of LiMn $_2$ O $_4$, this research provides valuable insights for optimizing the synthesis process and improving morphological control of the final product. Moreover, a deep understanding of flame synthesis mechanisms and the influence of reaction conditions contributes to refining cathode material fabrication for LIBs. These findings provide a theoretical foundation for optimizing industrial-scale production of battery materials, ultimately supporting the development of more efficient and sustainable low-carbon energy solutions.

2. Methodology

2.1. The simulation method

In this study, molecular dynamic (MD) simulations were conducted using the reactive force-field (ReaxFF) to explore the full dynamics of the reactions during flame synthesis. ReaxFF is parametrized in terms of the bond order, capable of describing the formation, dissociation and transition of the chemical bonds during chemical reactions [46]. The total energy of the system E_{system} is described by [47]:

$$E_{system} = E_{bond} + E_{over} + E_{under} + E_{lp} + E_{val} + E_{tor} + E_{vdWaals} + E_{Coulomb}$$
 (1)

Here, E_{system} encompasses both bonded and non-bonded interactions. The bonded interactions include the bond energy (E_{bond}), over-coordination energy (E_{over}), undercoordination energy (E_{under}), lone pair energy (E_{lp}), valence angle energy (E_{val}) and torsion angle energy (E_{tor}). Non-bonded interactions include both van der Waals energy ($E_{vdWaals}$) and Coulomb energy ($E_{Coulomb}$).

Bonded interactions are based on bond orders, BO_{ij} , expressed as [47]:

$$\begin{split} BO_{ij} &= BO_{ij}^{\sigma} + BO_{ij}^{\pi} + BO_{ij}^{\pi\pi} \\ &= exp \left[p_{bo1} \left(r_{ij} / r_0^{\sigma} \right)^{p_{bo2}} \right] + exp \left[p_{bo3} \left(r_{ij} / r_0^{\pi} \right)^{p_{bo4}} \right] + exp \left[p_{bo5} \left(r_{ij} / r_0^{\pi\pi} \right)^{p_{bo6}} \right] \end{split}$$

$$(2)$$

where r_{ij} is the distance between atom i and j, and p_{bo} terms are empirical parameters used to calculate the BO_{ij} . The contributions from sigma bonds, pi bonds and double pi bonds are distinguished. The bond orders are directly calculated for each pair of atoms, allowing for a smooth transition between non-bonded states and various bonded states (single, double or triple) during chemical reactions.

The ReaxFF force field has a high level of accuracy as its parameters are trained using quantum mechanics (QM) calculations [48]. During the development of the ReaxFF force field, a training set comprising atomic energetics derived from density functional theory (DFT) calculations is assembled, including optimized geometries, bond stretching energies, angle bending energies, reaction enthalpies, equation of state and charge distributions. These parameters were optimized to accurately reproduce the DFT-derived properties while also aligning closely with experimental values. For example, the ReaxFF force field used in this study has been parameterized to accurately capture the lattice constant of the stable metallic manganese phase, with a deviation of less than 3 % from experimental results. The predicted formation enthalpies of manganese oxides show less than 3 % deviation from DFT-calculated values. The force field also reliably predicts the lattice expansion and contraction of LiMn₂O₄ crystals, in agreement with both DFT and experimental results. The ReaxFF forcefield is noted for its transferability to various chemical environments irrespective of the specific applications for training the forcefield as it is trained to optimize atomic interactions among elements of interest. The ReaxFF MD simulation has been reported to study numerous reactive processes including fuel combustion [49,50], metal oxidation [51,52], metal sintering [53,54], and reactions of other energetic materials under extreme conditions [55–57].

In this study, all the ReaxFF MD simulations were performed using LAMMPS software [58] with the embedded REAXC package. The charge equilibration (QEq) method [59] was applied at every timestep to naturally capture changes in oxidation states and maintain charge neutrality throughout the simulation. The ReaxFF parameters containing C/H/O/Li/Mn elements were employed [60], which had been developed by enriching the well-established C/H/O parameters [47] and the lithium-based parameters [61] containing C/H/Li with additional optimizations for manganese interactions based on DFT calculations. The optimization process was based on fitting ReaxFF parameters to a DFT-derived training set of over 1500 structures, using a singleparameter search to minimize the deviation from quantum mechanical results. This force field has been applied to investigate various LiMn₂O₄ related systems, including the reactions at the LiMn₂O₄ cathode surface [44], Mn-ion dissolution [62], the self-healing cathode electrolyte interphase [45], and methane oxidation on manganese oxide [60]. Previous implementations have demonstrated its capability in describing C/H/O/Li/Mn interactions across various situations, such as liquid solutions, surface reactions, thermal decomposition and oxidation, while also providing insights into fundamental mechanical properties. Therefore, we employed this ReaxFF force field [60] to study the formation of LiMn₂O₄ nanoparticles from liquid precursors during flame synthesis, aiming to elucidate the atomistic reaction mechanisms and formation pathways of this promising Li-ion battery cathode material.

2.2. Simulation setup

To closely simulate the experimental conditions of flame spray pyrolysis (FSP), where precursor solutions are sprayed into the combustion

chamber, a precursor droplet model was constructed. The precursor consists of lithium acetylacetonate and manganese (III) acetylacetonate at a Li:Mn molar ratio of 1:2, with a concentration of 0.6 M and 1.2 M for Li and Mn, respectively. This composition reflects the stoichiometry of LiMn₂O₄, resulting in a total metal concentration of 1.8 mol/L. This concentration is at the high end but within the upper bound reported in experimental studies [17] in order to ensure that a sufficient number of metal atoms are present in the simulation domain, facilitating interactions and reaction events within the timescale of MD simulations. In practical FSP experiments, precursor metal concentrations are often lower, as high concentrations may lead to increased viscosity and affect spray behaviors that are not considered in the present study. The solvent consists of a mixture of toluene and 2-ethylhexanoic acid in a volume ratio of 1:2. The composition of the precursor and the concentration of metals closely align with the experimental setup reported by Ernst and Patev [17,30,63], who employed a similar precursor mixture for the FSP synthesis of LiMn₂O₄ nanoparticles. Further details on the precursor composition can be found in the Supplementary Information, Table S1.

The initial MD configuration of the precursor nanodroplet was constructed using the PACKMOL program [64], producing a droplet with a diameter of 61.4 Å and a density of 1.2016 g/cm³. The atom distributions within the droplet were then optimized [65], with the constructed droplet shown in Fig. 1a. To eliminate any artifacts introduced during the construction of the initial geometry, the droplet was relaxed at 300 K under the isothermal-isobaric (NPT) ensemble with a pressure of 1 atm for 0.06 ns, until the potential energy of the system stabilized. The system was subsequently equilibrated under the canonical (NVT) ensemble at 300 K for an additional 0.06 ns. The corresponding temperature and potential energy evolution during optimization are shown in Fig. S1. After equilibration, the droplet was considered fully relaxed, as illustrated in Fig. 1b, and the distribution of Li and Mn atoms within the droplet is shown in Fig. 1c, demonstrating their uniform dispersion within the droplet. The optimized droplet has a diameter of 6.2 nm. While smaller than typical experimental droplets (micrometer scale)

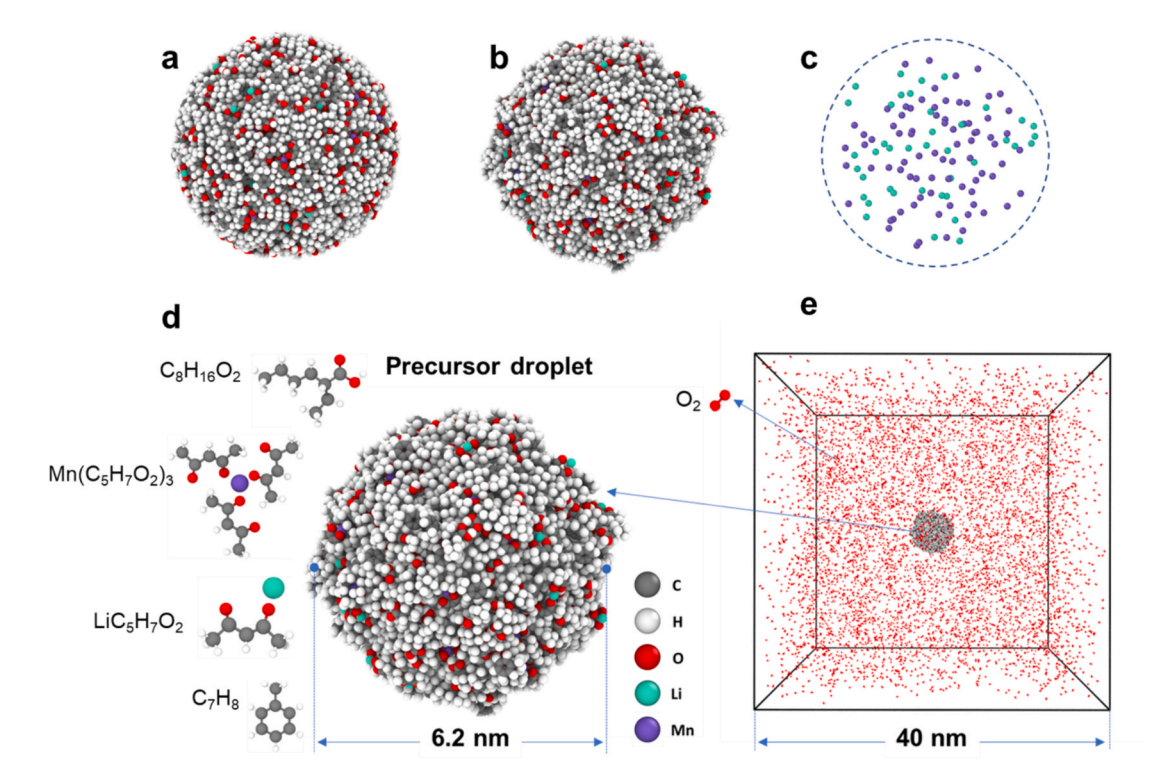


Fig. 1. (a) Initial configuration of the precursor nanodroplet after construction, (b) after relaxation, and (c) the distribution of Li (green) and Mn (purple) atoms within the droplet (dashed circle). (d) Molecular structures of the solvent and solute components of the droplet, including $C_8H_{16}O_2$, $Mn(C_5H_7O_2)_3$, $LiC_5H_7O_2$, and C_7H_8 , and (e) illustration of the simulation system, with the droplet placed at the center of a 40 nm cubic box surrounded by O_2 molecules (red). (For interpretation of the references to colour in this figure legend, the reader is referred to the web version of this article.)

[66], nanoscale droplets may form via microexplosions or fragmentation in FSP [67–69]. This size allows full simulation of the FSP process within feasible computational time.

The prepared droplet was placed at the center of a periodic cubic box with a side length of 40 nm. Subsequently, 6663 O_2 molecules were randomly distributed within the box to achieve an air–fuel ratio of 1, resulting in a total of 27,781 atoms within the simulation box. The initial condition of the simulation box is shown in Fig. 1e, while detailed molecular structures of both the solvent and solute within the droplet, along with oxygen molecules, are shown in Fig. 1d. Periodic boundary conditions were applied in all directions (x, y, z). Following energy minimization and equilibration, the initial temperature of the surrounding oxygen was set to 1000 K, while the droplet was maintained at 300 K to simulate its entry into the flame.

MD simulations were performed using the NVE ensembles until the system reached the target combustion temperature (T_c) . Simulations were conducted at four different T_c (1500, 2000, 2500, and 3500 K), in the range of experimental combustion temperature [70,71], with all systems starting from the same initial NVE ensemble, as shown in Fig. 2. After maintaining each system at its respective T_c for 1 ns, the system was gradually cooled using the NVT ensemble with the Nosé-Hoover thermostat, applying a damping constant of 100 fs. The rapid combustion and slower cooling due to air entrainment were based on experimental thermocouple measurements [70]. The system was then maintained at room temperature (300 K) until the total simulation time reached 10 ns. The temperature profiles of the system for the four cases with different T_c over a total simulation time of 10 ns are shown in Fig. 2. All visualizations in this study were generated using the Open Visualization Tool (OVITO) software [72], and reaction pathways were analyzed using the Chemical Trajectory Analyzer (ChemTraYzer) scripts [73]. A detailed summary of the molecular dynamics setup can be found in Table S2.

3. Results and discussion

3.1. The dynamic process of FSP

Fig. 3a presents the evolution of the O_2 number (red line, left axis) and system temperature (black line, right axis) over the 10 ns simulation for a combustion temperature of 2500 K. Since the process of FSP is accompanied by decomposition and combustion, monitoring the oxygen molecule count is crucial for tracking the reaction progress. To delve

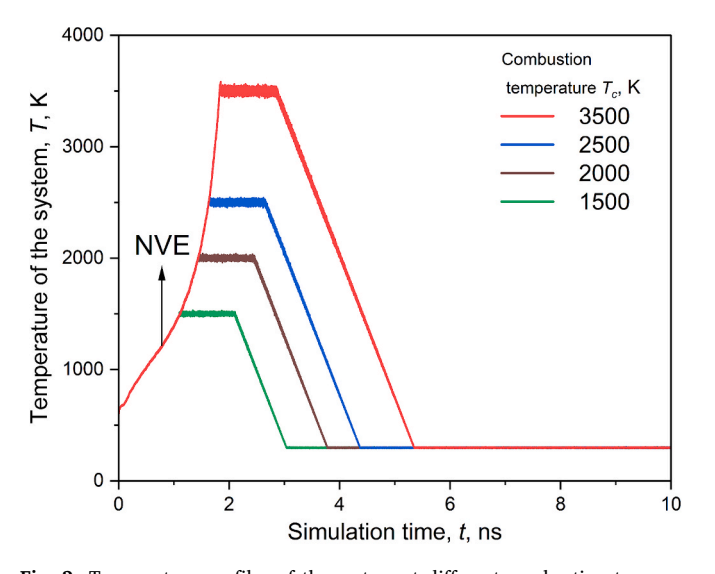


Fig. 2. Temperature profiles of the system at different combustion temperatures (T_c) over a total simulation time of 10 ns, with the initial NVE ensemble stage indicated.

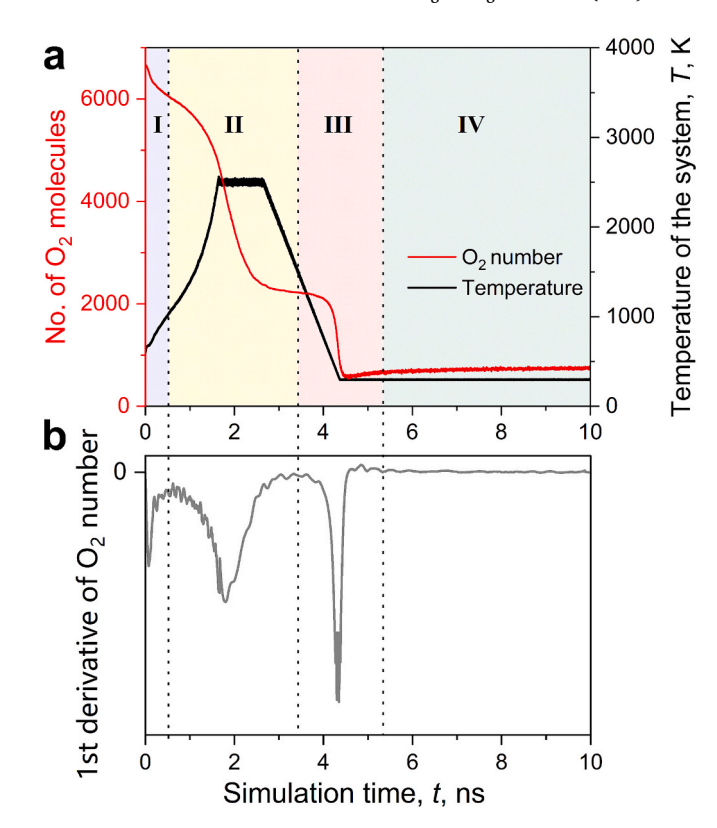


Fig. 3. FSP process at a combustion temperature of 2500 K: (a) Temporal evolution of O_2 number (red line, left axis) and system temperature (black line, right axis) over the 10 ns FSP process. The four stages (I–IV) are highlighted in distinct colors. (b) First derivative of O_2 number with respect to time, with dashed lines marking transitions between key reaction phases. (For interpretation of the references to colour in this figure legend, the reader is referred to the web version of this article.)

deep into the reaction dynamics, the first derivative of the $\rm O_2$ number with respect to time is shown in Fig. 3b. Three prominent peaks are observed, indicating distinct phases of oxygen change, which correspond to major transitions in the combustion process. These peaks partition the FSP process into four stages, which are highlighted by the shaded areas in Fig. 3a. The left boundary of each peak is determined as the first intersection between the derivative curve and a fitted baseline obtained via peak analysis in OriginLab [74]. Corresponding figures and stage divisions for combustion temperatures of 1500, 2000, and 3500 K are provided in Figs. S2–S4. In the following sections, the detailed reaction mechanisms within each stage will be analyzed to further elucidate the combustion chemistry and nanoparticle formation.

3.2. Detailed mechanisms at four distinctive stages

3.2.1. Stage I: Evaporation & initial decomposition

According to Fig. 2, all four cases undergo the same Stage I, regardless of combustion temperature. During Stage I, the number of O_2 molecules decreases significantly, while the system temperature rapidly rises from 500 K to approximately 1000 K. This occurs because the surrounding oxygen, initially at 1000 K, reacts intensely with the precursor droplet (initially at 300 K) upon contact, oxidizing its molecules fiercely and releasing heat in the process. As shown by the peak in Fig. 3b, the oxygen reaction rate increases sharply at first and then gradually slows.

Fig. 4a shows the evolution of non-metallic solvents and their reaction products. Both toluene and 2-ethylhexanoic acid steadily decrease as they react with oxygen, forming smaller fragments such as CO, CO_2 , H_2O , H_2O_2 , and others. By the end of Stage I, H_2O and CO are the most

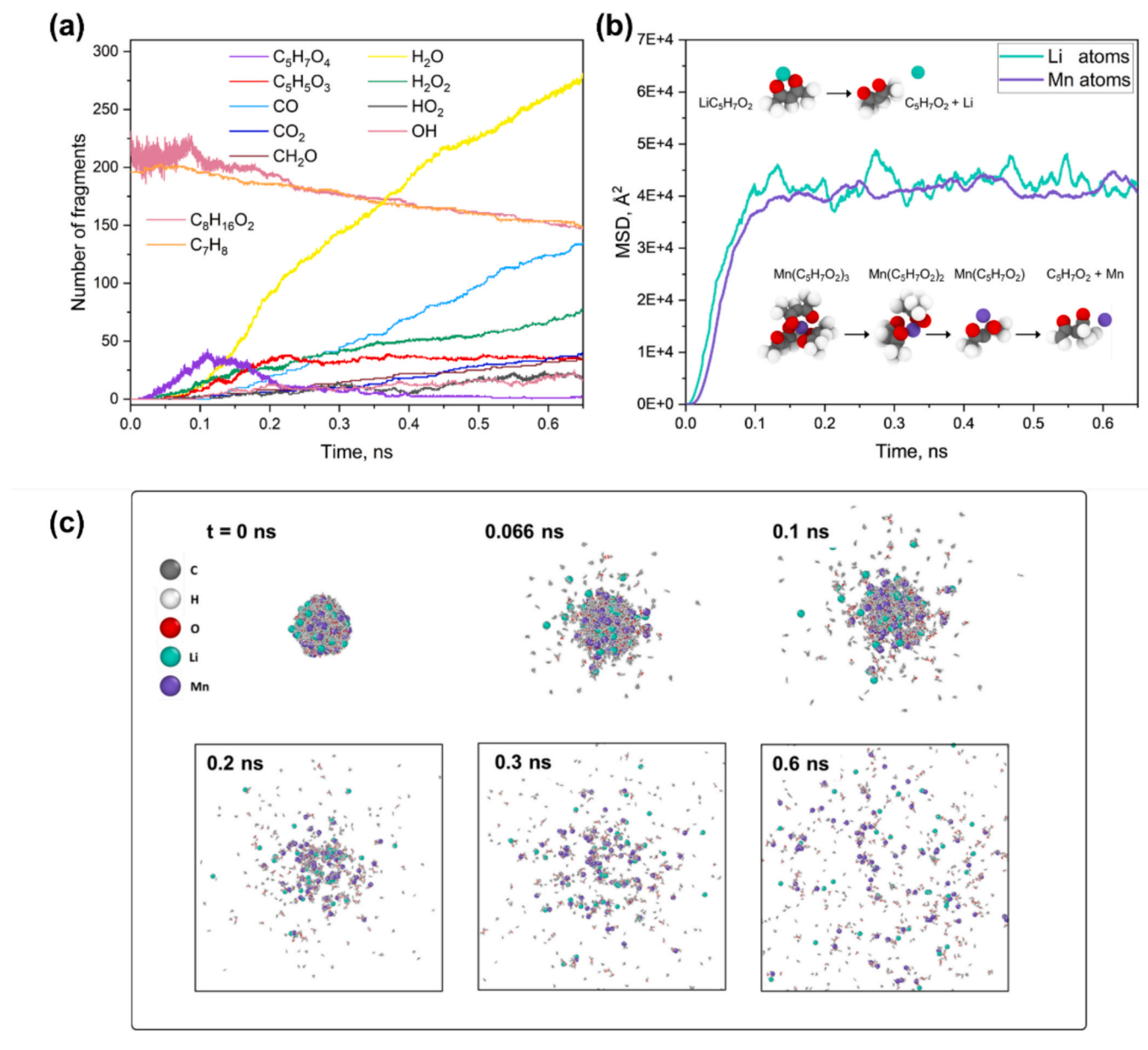


Fig. 4. (a) Time evolution of the number of main non-metallic fragments in the simulation box. (b) Mean square displacement (MSD) of Li and Mn atoms during Stage I, highlighting simplified C₅ group loss pathways. (c) Snapshots of the precursor droplet during Stage I, showing the evaporation process and the diffusion of Li and Mn atoms, with magnified views of Li and Mn atoms for clearer visualization.

abundant newly formed non-metallic products. Intermediate species of the C₅ group, such as C₅H₇O₄ and C₅H₅O₃, both have been found during oxidation of acetylacetone [75], show a brief increase followed by a decrease. This is due to the release of C5H7O2 fragments during precursor decomposition, as illustrated by the snapshots of simplified C5 group loss pathways in Fig. 4b. The Li-containing and Mn-containing precursor molecules contain different numbers of C5 groups due to their valence, which facilitates the decomposition and diffusion of Licontaining species. This is reflected in the slightly higher mean squared displacement (MSD) of Li atoms over time in Fig. 4b. Additionally, the lower atomic mass of Li contributes to its higher MSD value [76]. Snapshots in Fig. 4c illustrate the evaporation state of the precursor droplet during Stage I, with magnified views of Li and Mn atoms showing their dispersion. Snapshots captured at 0.066, 0.1, and 0.2 ns clearly show that Li atoms diffuse farther than Mn atoms during the early stages of Stage I. By 0.6 ns, however, Mn atoms have spread uniformly throughout the simulation box, demonstrating that they eventually achieve complete diffusion by the end of Stage I. Full snapshots of the entire simulation box during this stage, provided in Fig. S5a, further illustrate how the evaporated precursor mixes with the surrounding $\rm O_2$ gas. It is noted that experimental studies have shown that microexplosions frequently occur in FSP droplets due to internal vapor bubble nucleation and rapid shell rupture, which significantly enhance precursor release and gas-phase interactions [77–79]. Such microexplosion phenomena have also been observed by He and Luo [68,69] in their MD simulations, under certain combinations of precursor droplet composition, ambient temperature and pressure. In the present study, no abrupt fragmentation is observed during evaporation in Stage I (Fig. S5b), and no micro-explosions occur. This is due to the specific present setup, where internal superheating and pressure buildup are not sufficient to trigger micro-explosions.

Fig. 5 illustrates the evolution of major Li-containing species during Stage I. As shown in Fig. 5a, most Li atoms initially exist as $LiC_{13}H_{23}O_4$ (Li(acc)($C_8H_{16}O_2$)), a species formed by the attachment of toluene to lithium acetylacetonate, as depicted in Fig. 5c. In addition, lithium acetylacetonate can combine with another acetylacetonate molecule to

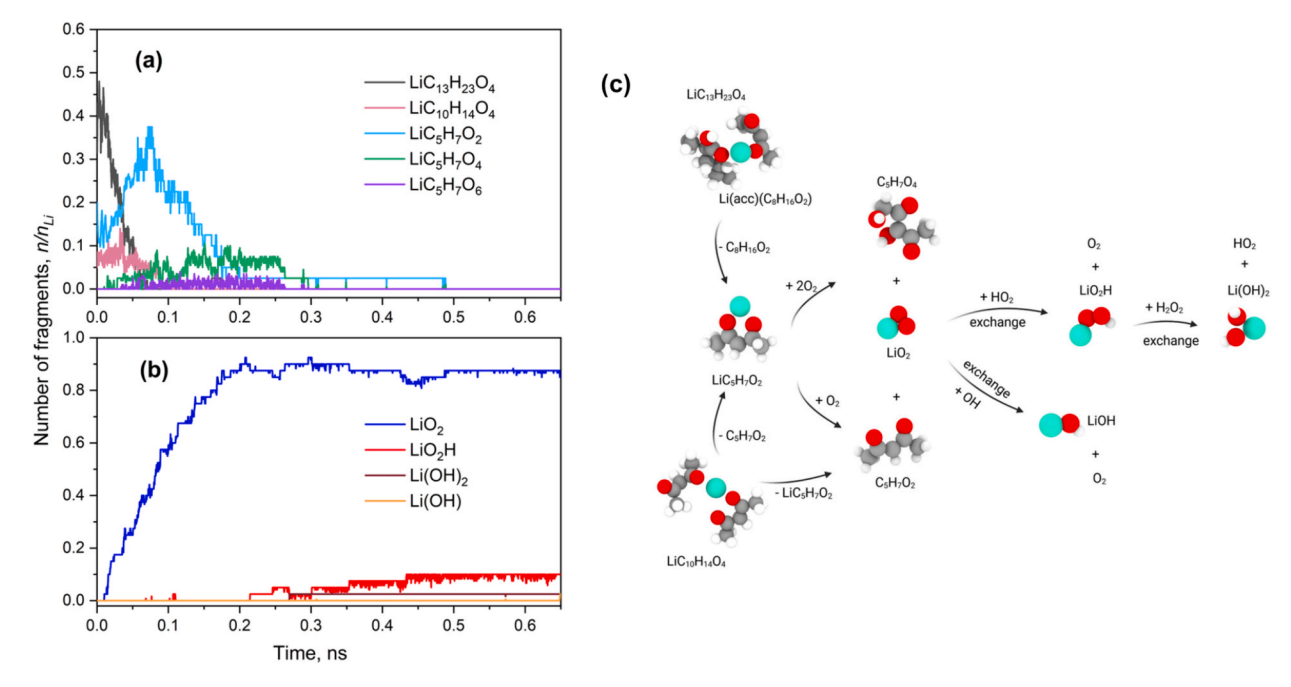


Fig. 5. Time evolution of the normalized number (n/n_{Li}) of Li-containing species $LiC_xH_yO_z$ (y, z>0) with (a) x>0 and (b) x=0. (c) Illustration of the key decomposition pathways of Li-containing species during Stage I.

form $LiC_{10}H_{14}O_4$. Both attached species gradually lose their organic groups and revert to lithium acetylacetonate, as indicated by the initial increase in its concentration (blue line in Fig. 5a).

During Stage I, lithium acetylacetonate continuously decomposes upon reacting with O_2 , releasing C_5 groups in the form of $C_5H_7O_2$ or $C_5H_7O_4$, and producing LiO_2 as the primary product. Fig. 5b shows that LiO_2 increases sharply and becomes the dominant Li-containing species throughout Stage I, significantly exceeding the concentrations of other species. Subsequently, LiO_2 can further react with environmental species—such as by exchanging groups with HO_2 to form LiO_2H while releasing O_2 . Although minor amounts of $Li(OH)_2$ and Li(OH) are also produced from reactions involving LiO_2 , their concentrations remain

much lower, allowing ${\rm LiO}_2$ to accumulate and dominate as the primary Li-containing species.

Fig. 6 presents the evolution of major Mn-containing species during Stage I. As depicted in Fig. 6a, about 55 % of the Mn atoms remain as manganese (III) acetylacetonate, which aligns with its initial abundance in the precursor. This species can further transform by incorporating an H radical to form $MnC_{15}H_{22}O_6$ or by adding two O radicals to form $MnC_{15}H_{21}O_8$, as illustrated in Fig. 6c. Around 10 % of manganese (III) acetylacetonate initially bond with toluene to form $MnC_{23}H_{37}O_8$. Over time, these toluene attachments are lost, similar to the behavior observed for Li-containing species in Fig. 5. The Mn-containing species bearing C_{15} groups subsequently decompose by releasing a C_5 fragment,

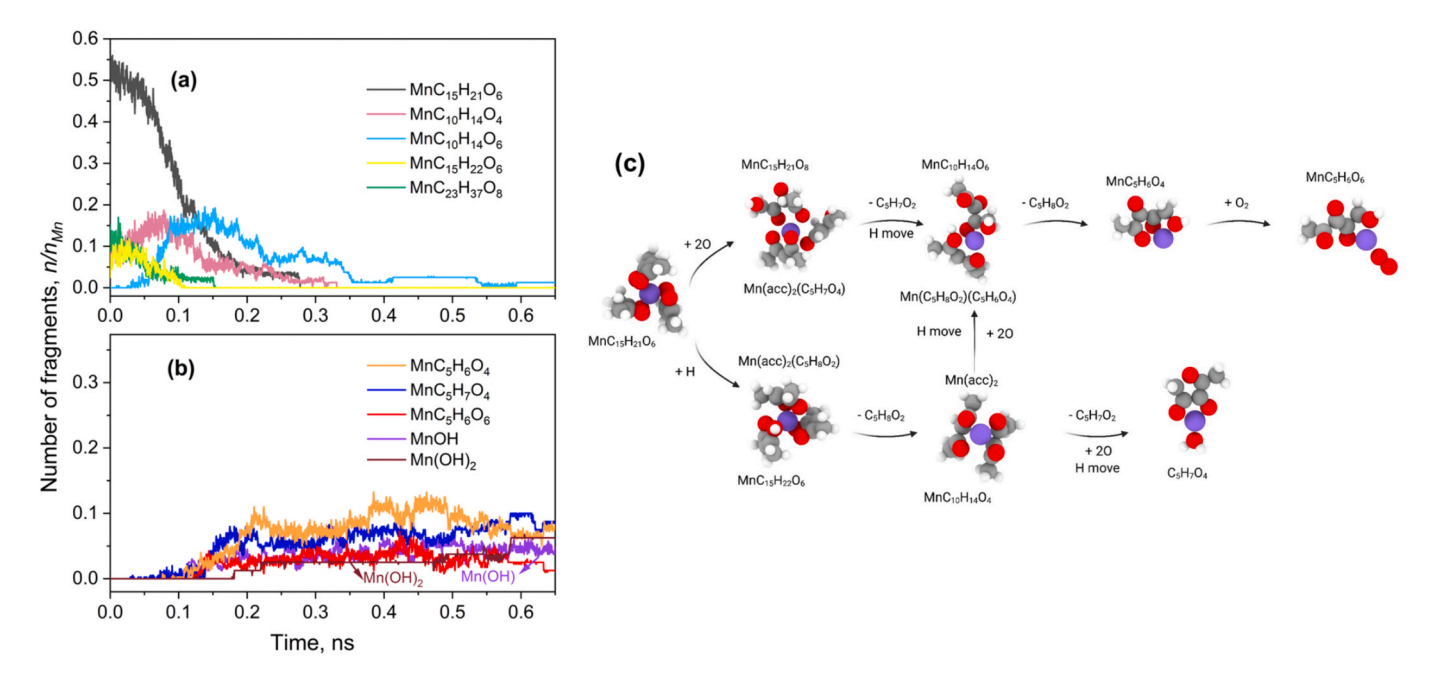


Fig. 6. Time evolution of the normalized number (n/n_{Mn}) of Mn-containing species Mn $C_xH_yO_z$ (y, z > 0) with (a) x > 5 and (b) $x \le 5$. (c) Illustration of the key decomposition pathways of Mn-containing species during Stage I.

either as C₅H₇O₂ or C₅H₈O₂, leading to the formation of MnC₁₀H₁₄O₆ or MnC₁₀H₁₄O₄. Moreover, MnC₁₀H₁₄O₄ can further convert to MnC₁₀H₁₄O₆ via pathways that involve breaking C-H bonds and forming new C-O and H-O bonds (Fig. 6c). Although the concentration of Mn species with C₁₀ groups initially increases, it later decreases as these species release an additional C₅ group. By the end of Stage I, the dominant Mn-containing species are MnC5H6O4, MnC5H6O6, and MnC₅H₇O₄. Furthermore, a fraction of Mn atoms completely lose their carbon groups, resulting in approximately 5 % of Mn existing as Mn(OH) and another 5 % as Mn(OH)2, as shown in Fig. 6b. The stepwise release of C₅ groups from Mn-containing precursors observed in our simulations is consistent with experimental results reported by Lalancette et al. [80], who studied the thermal decomposition of Mn(acac)3 using thermogravimetric analysis (TGA), differential scanning calorimetry (DSC), and mass spectrometry (MS). Their results show a two-step mass loss process, each with approximately 20 % mass loss, indicating sequential ligand detachment from Mn(acac)₃.

In comparison, Mn-containing species exhibit more complex decomposition pathways, likely due to their higher valence. By the end of Stage I, all Li-containing species have fully decomposed into smaller fragments that no longer contain any C groups. In contrast, a significant fraction of Mn-containing species still retain one C_5 group, highlighting the slower and more intricate decomposition process for Mn species.

3.2.2. Stage II: Combustion-driven oxidation

As the system surpasses 1000 K, all cases transition into Stage II, signaling a shift from mild oxidation to intense combustion. During this stage, the temperature rises sharply [81] until reaching the combustion temperature (T_c), where it plateaus for 1 ns. This plateau represents the period in which the mixed precursors undergo vigorous combustion

[82], reaching the outer flame region. Subsequently, the temperature begins to decline, indicating the departure of high-temperature combustion gases from the flame, while residual thermal energy maintains the system above 1000 K [82]. By the end of Stage II, temperatures remain elevated, indicating that combustion-driven oxidation dominates the process.

The dynamics of oxygen consumption further elucidate the combustion intensity. During Stage II, the number of O_2 molecules declines sharply, with the O_2 consumption rate exhibiting a distinct peak (Fig. 3b, Figs. S2–4b). This peak signifies an initial acceleration in oxidation reactions, followed by a deceleration as reactants are depleted. Notably, the magnitude of this peak diminishes at lower T_c values (Fig. 3b, Figs. S2–4b), reflecting reduced maximum oxidation rates under milder combustion conditions. Total oxygen consumption also varies with T_c . By the end of Stage II, fewer than 2000 O_2 molecules remain at O_2 molecules remain at O_3 molecules remain at O_4 molecules remain at O_5 molecules remain at O_6 molecules remain at O_6

The duration of Stage II also differs depending on the combustion temperature, as higher combustion temperatures require prolonged heating to reach $T_{\rm c}$ [71] This relationship underscores the interplay between thermal energy input and reaction kinetics, where elevated temperatures not only intensify oxidation but also prolong the active combustion phase.

Fig. 7 compares the evolution of major Li-containing species at $T_c = 3500$, 2500, and 1500 K during Stage II, with corresponding data for $T_c = 2000$ K provided in Fig. S6. As noted in Stage I, LiO₂ becomes the predominant Li-containing species following evaporation and initial decomposition. As the temperature increases during Stage II, LiO₂ continuously decreases. One major reaction involves LiO₂ combining

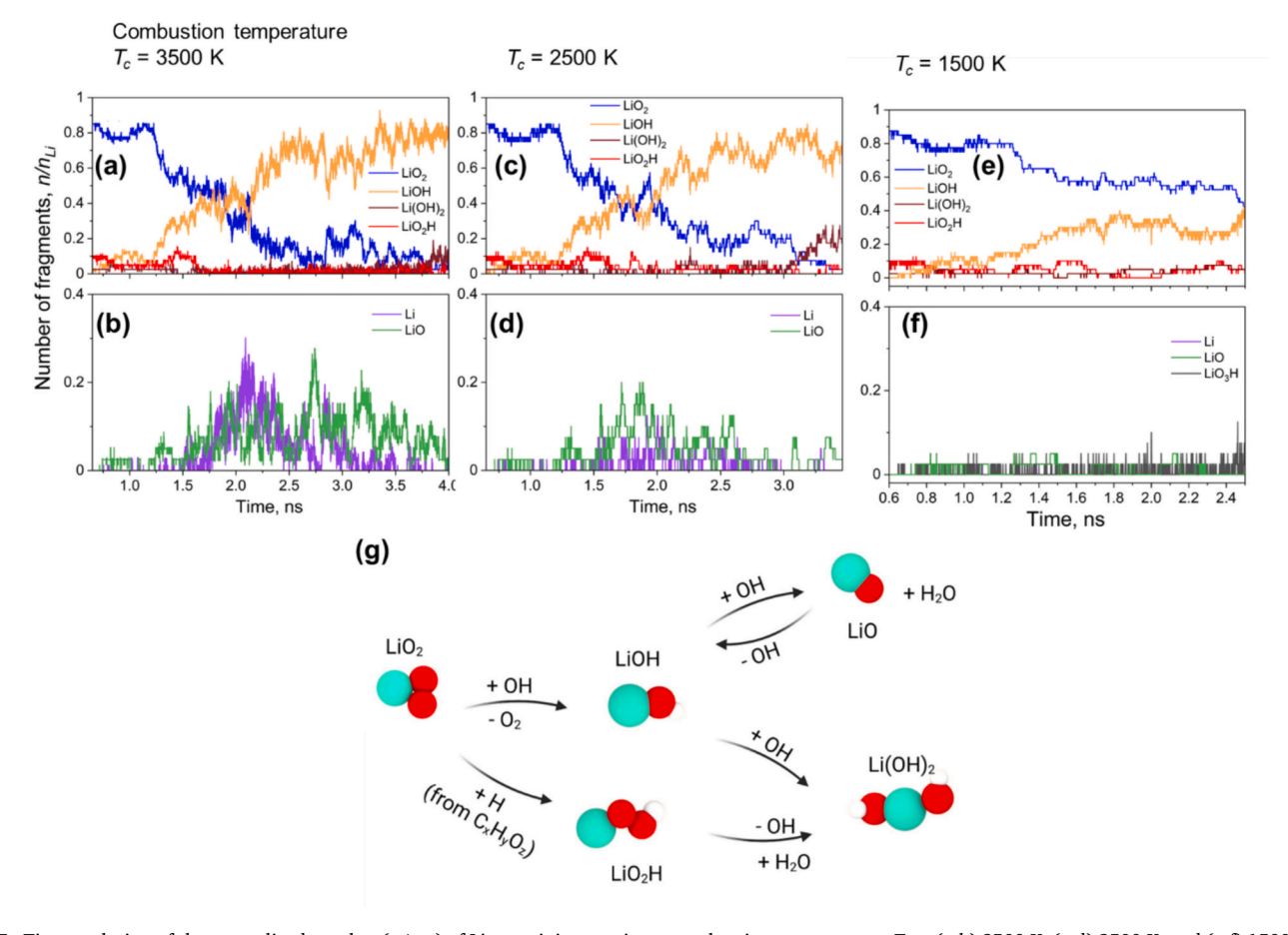


Fig. 7. Time evolution of the normalized number (n/n_{Li}) of Li-containing species at combustion temperatures $T_c =$ (a-b) 3500 K, (c-d) 2500 K, and (e-f) 1500 K. (g) Illustration of the key reaction pathways of Li-containing species during Stage I.

with OH, releasing O_2 and forming LiOH (the pathway shown at the top of Fig. 7g). This reaction dominates across all combustion temperatures, as evidenced by the continuous rise of LiOH (orange lines in Fig. 7a, c and e). Higher temperatures strongly promote this transition: over 80 % of Li transforms into LiOH by the end of Stage II at $T_c = 3500$ K (Fig. 7a), while only 50 % forms at $T_c = 1500$ K (Fig. 7c).

Another reaction involves LiO_2 adding an H radical from environmental carbon groups to form LiO_2H (the reaction shown at the bottom of Fig. 7g). However, this reaction is less significant compared to LiOH formation. Both LiOH and LiO_2H can further react by adding or releasing OH to form Li(OH)_2 . The formation of Li(OH)_2 is more prominent at higher temperatures ($T_c = 2000-3500 \text{ K}$, Fig. 7a and c, Fig. S6), while at $T_c = 1500 \text{ K}$, almost no Li(OH)_2 is observed (brown line in Fig. 7e), suggesting that the pathway leading to Li(OH)_2 formation is less favorable at lower temperatures.

Throughout the reactions, Li and LiO act as important intermediates (as shown by the purple and green line in Fig. 7b, d and f, and Fig. S6), appearing primarily in the middle of Stage II but disappearing by the end. The concentration of Li and LiO decreases as T_c decreases, reflecting reduced reaction rates at lower combustion temperatures.

Fig. 8 compares the evolution of major Mn-containing species at T_c = 3500, 2500, and 1500 K during Stage II, with corresponding data for T_c = 2000 K provided in Fig. S7. As shown in Fig. 6, Mn-containing species

with one C_5 group, such as $MnC_5H_6O_4$ and $MnC_5H_7O_4$, dominate by the end of Stage I. During the early period of Stage II, these species decompose steadily, as shown in Fig. 8a for $T_c=2500$ and 3500 K, where their initial decomposition period overlaps.

The decomposition of $MnC_5H_6O_4$ occurs through the breaking of a C—OH bond within the C_5 group, forming a Mn—OH bond and producing $Mn(OH)_2$, along with the release of the C_5 group (illustrated at the top of Fig. 8c). $MnC_5H_7O_4$ follows a slightly different pathway, initially losing an H radical to form an allotrope of $MnC_5H_6O_4$ (Fig. 8c, bottom), then releasing its C_5 group to form MnOH. Fig. 8c illustrates the main decomposition pathways, while some nominal intermediates are shown in Fig. 8b, representing alternative reaction pathways.

Mn(OH)₂ can further decompose by losing an H₂O molecule, forming MnO, which acts as a key intermediate. As shown in Fig. 8e, h, and Fig. S7d, the peak concentration of MnO decreases as T_c decreases, indicating that higher temperatures favor its formation and subsequent reactions. Similarly, Mn(OH) and Mn also serve as important intermediates, and their peak concentrations are lower with decreasing T_c (Fig. 8e, h, and Fig. S7d). At $T_c = 1500$ K, the concentration of Mn(OH) and Mn are significantly lower, and the main intermediates shift to Mn (OH)₂ and MnO₂H₃ (Fig. 8k).

These intermediates then react further to form MnO_2H , MnO_2 , and $Mn(OH)_2$ as the primary products at $T_c=2000-3500$ K. The

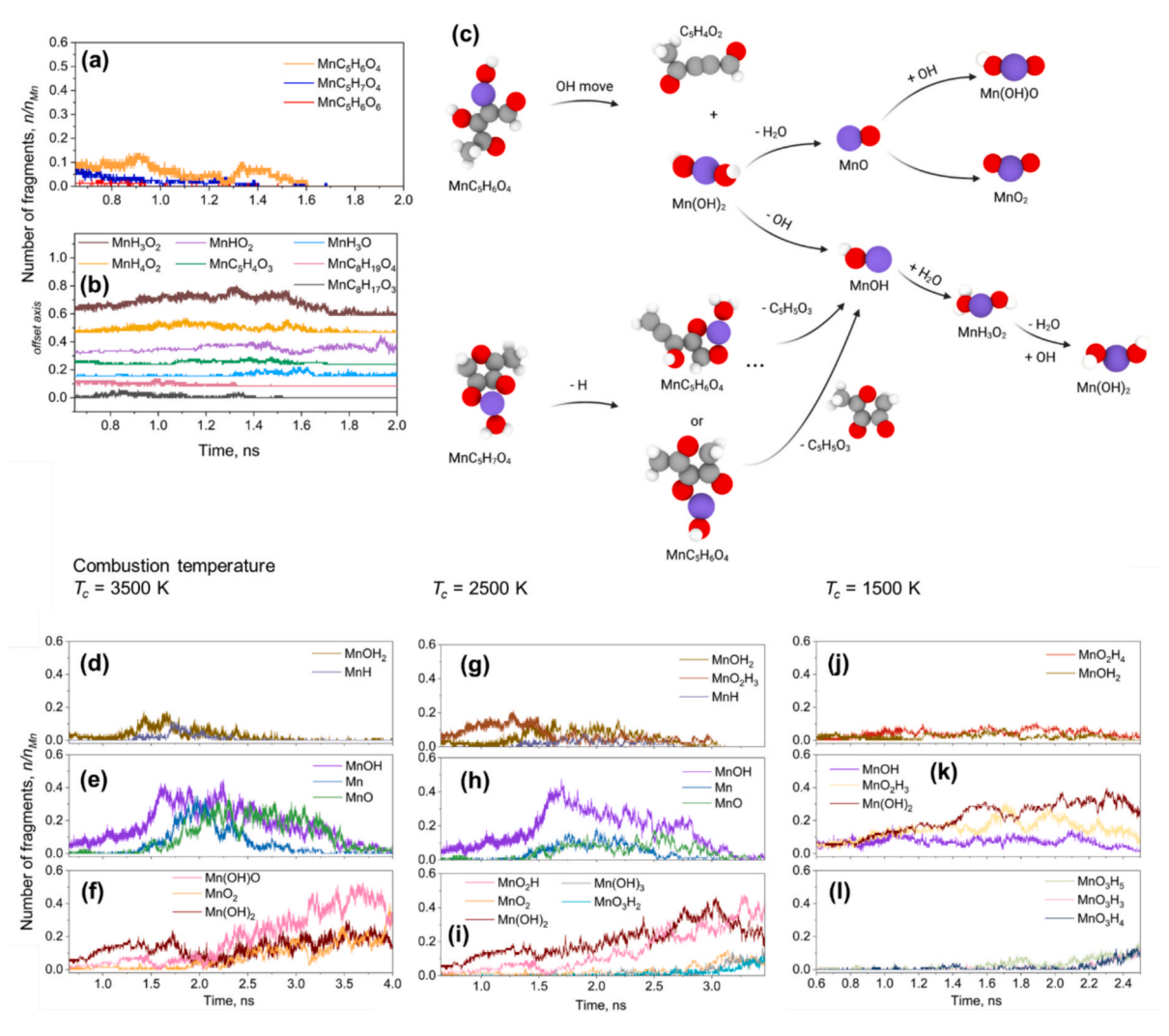


Fig. 8. Time evolution of the normalized number (n/n_{Mn}) of Mn-containing species during (a-b) initial decomposition in Stage II. (c) Illustration of the key reaction pathways of Mn-containing species. Evolution of n/n_{Mn} of Mn-containing species throughout Stage II at combustion temperatures of (d-f) 3500 K, (g-i) 2500 K, and (j-1) 1500 K.

concentrations of MnO₂H and MnO₂ decrease with decreasing T_c , while Mn(OH)₂ increases. By the end of Stage II, MnO₂ (33 %) and MnO₂H (29 %) are the dominant products at $T_c = 3500$ K (Fig. 8f), while MnO₂H (34 %) and Mn(OH)₂ (22 %) dominate at $T_c = 2500$ K, with less MnO₂ (12 %) (Fig. 8i). At $T_c = 2000$ K, the main products are MnO₃H₄ (22 %), MnO₃H₃ (21 %), MnO₃H₅ (15 %), and Mn(OH)₂ (15 %) (Fig. S7e). At $T_c = 1500$ K, Mn(OH)₂ accounts for 25 %, and other products are MnO₃H₅ (15 %), and MnO₃H₃ (12 %) (Fig. 8l), which are also observed at $T_c = 2000$ K (Fig. S7f). Overall, the oxidation state of Mn-containing species decreases with decreasing T_c .

The combustion temperature plays a crucial role in determining the reaction pathways, intermediate stability, and final product distributions of Mn-containing species. Higher combustion temperatures favor the formation of oxidized products such as MnO2 and MnO2H, while lower temperatures result in the dominance of hydroxylated species like Mn(OH)₂. This trend occurs because, at higher temperatures, both dehydroxylation and dehydrogenation are thermodynamically favored [83], and oxidation reaction rates are significantly enhanced. In contrast, lower temperatures slow these processes, leading to the persistence of intermediates and the accumulation of hydrogen in the final products. The higher oxidation state of Mn after high-temperature treatment has also been confirmed through calcination experiments [84]. It is worth noting that the use of a Mn³⁺-based precursor in our simulation aligns more closely with the aimed oxidation states for LiMn₂O₄. Fig. 8 further suggests that sufficient residence time at high temperature (e.g., t > 4.0 ns at $T_c = 3500$ K) is critical for complete ligand detachment and subsequent oxidation.

Figs. 7 and 8 show only the main species with high concentrations to illustrate the major reaction pathways. However, at high temperatures, many more types of Li-containing and Mn-containing species exist in the combustion chamber. These species can dynamically convert and reconvert to each other, as shown by the reaction network for Li and Mn in Fig. S8 generated by ChemTraYzer [85] during a period when the system temperature is kept at 2500 K for 1 ns (the high-temperature plateau at T_c).

Stage II is characterized by the vigorous combustion of organic species, accompanied by the decomposition and oxidation of both Liand Mn-containing species. While T_c primarily influences the decomposition extent of LiO_2 and the resulting product concentrations, it does not significantly alter the main reaction pathways or key intermediates for Li-containing species. In contrast, for Mn-containing species, T_c not only affects the concentration of intermediates but also plays a crucial role in shaping reaction pathways by influencing the transformation of hydroxylated species, ultimately leading to variations in the final products [84]. This suggests that Mn-containing species exhibit greater temperature sensitivity during FSP compared to Li-containing species.

3.2.3. Stage III: Nucleation

In Stage III, the system temperature gradually decreases from approximately half of T_c (Fig. 3a and Fig. S2–S4a) to room temperature. During this stage, the number of O₂ molecules undergoes another sharp decline, with the O2 consumption rate exhibiting a distinct peak. This peak represents the most significant oxygen consumption event for T_c < 2500 K and the second largest for $T_c = 3500$ K (Fig. 3b, Figs. S2–S4b). Fig. 9 presents the evolution of normalized O_2 concentration (n/n_{t0}) during FSP for different T_c cases. For $T_c > 2000$ K, the decrease in O_2 during Stage III stabilizes at approximately $n/n_{t0} = 0.1$, with slightly higher residual O_2 levels at higher T_c . However, at $T_c = 1500$ K, a more substantial O2 depletion during Stage III leads to a final concentration of around 0.2, which is significantly higher than in other T_c cases. This cooling-driven oxidation phase corresponds to the stage in FSP when combustion products leave the flame and cool down until reaching the particle collection region [20]. The continued reaction of residual oxygen with intermediate species plays a crucial role in determining the final oxidation state and structural evolution of the synthesized nanoparticles.

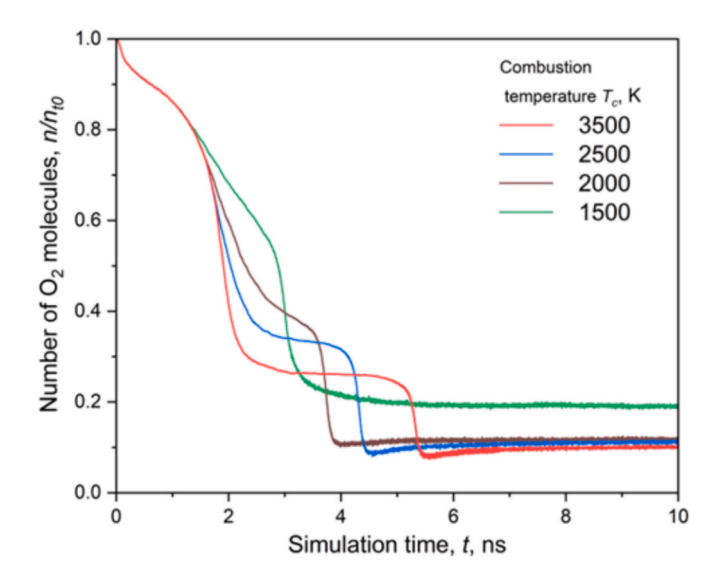


Fig. 9. Temporal evolution of O_2 concentration (n/n_{t0}) at different combustion temperatures (T_c) over the 10 ns FSP process.

As previously discussed, the combustion temperature (T_c) strongly influences the product species by the end of Stage II. Fig. 10 shows the evolution of Mn-containing species in Stage III, ith data for $T_c=2000~\rm K$ provided in Fig. S9. Here, after entering Stage III, those oxidized species such as MnO₂H, MnO₂, and MnO₂H₃, existing in all T_c cases, decrease in concentration during this stage. Mn-containing species begin to incorporate additional oxygen and hydrogen, resulting in an increase in more highly oxidized species (Mn_xO_yH_z, where x > 2 and y > 3) after a brief period in Stage III.

Fig. 11a illustrates a typical cluster formation pathway for Mncontaining species at $T_c = 2500$ K. The process initiates with the transformation of MnO2 into MnO(OH) via the substitution of one oxygen atom with an OH group. This intermediate undergoes further hydrogenation, forming Mn(OH)2 at 3.75 ns, which subsequently converts into MnO₃H₄ at 3.92 ns. MnO₃H₄ (or Mn(OH) ₃ upon the loss of an H atom) serves as a key intermediate to the emergence of small Mn crystal clusters, supported by the peak concentrations of MnO₃H₄ and Mn(OH)₃ observed at 3.8-4.2 ns (Fig. 10c-d) and 2.6-3.0 ns (Fig. 10e-f). As MnO₃H₄ continues to evolve, it incorporates an additional OH group to form MnO_4H_5 at 4.07 ns, a crucial intermediate, particularly at $T_c =$ 3500 K and 2500 K (Fig. 10b and 10d). However, at $T_c = 1500$ K, the corresponding intermediate is MnO₄H₇ (Fig. 10f), indicating a higher degree of hydroxylation under lower temperatures. With continued oxygenation, Mn forms a tetrahedral MnO₄H₅ unit at 4.07 ns and further transforms into MnO₅H₇ at 4.14 ns.

This initial Mn crystal cluster subsequently interacts with neighboring clusters. By 4.80 ns, two Mn-containing clusters come into close proximity, and at 4.91 ns, they merge through the formation of O—O bonds, resulting in a $\rm Mn_2O_{11}H_{21}$ structure. As the simulation progresses, this structure undergoes further compaction, reaching a more thermodynamically stable configuration by 10 ns. Overall, the crystallization of Mn-containing species during Stage III involves a dynamic interplay of Mn—O and O—O bond breaking and reformation, progressively driving the system toward more ordered and thermodynamically stable structures.

In contrast, the formation pathway for Li-containing species is relatively simple. Fig. 12a, c, and e and Fig. S10a show that Stage III is marked by a gradual decrease of the main oxidized Li-containing species—LiOH for $T_c=3500$, 2500 and 2000 K and LiO₂ for $T_c=1500$ K. The primary intermediates include Li(OH)₂, LiO(OH), and LiO₂, with Li generally exhibiting a lower oxidation extent at higher T_c . As depicted in the reaction pathway in Fig. 11b, LiOH initially undergoes further oxidation to form LiO(OH) (an intermediate clearly seen in Fig. 12c). For

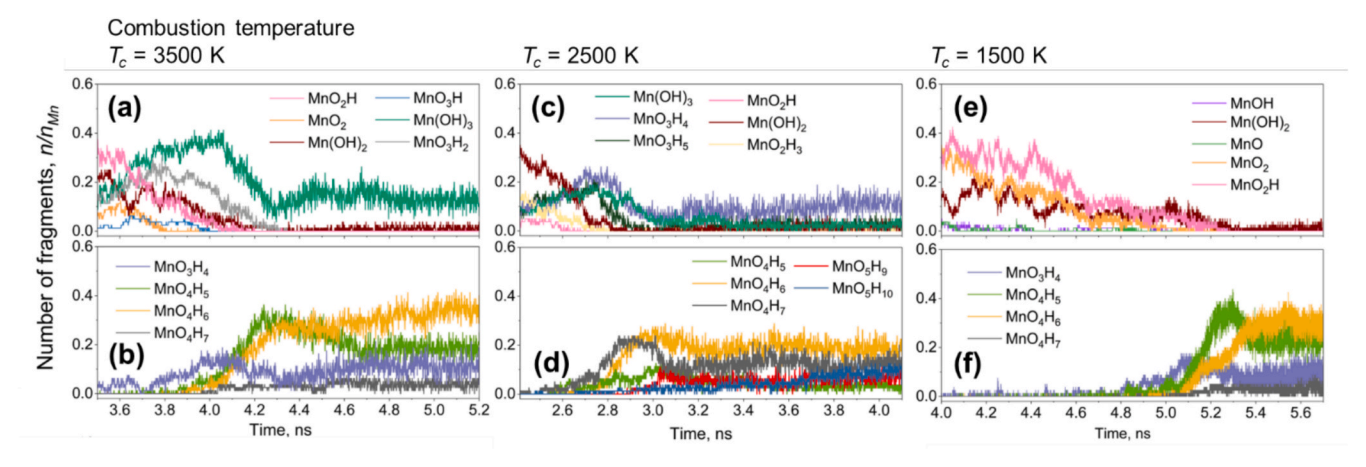


Fig. 10. Time evolution of the normalized number (n/n_{Mn}) of Mn-containing species throughout Stage III at combustion temperatures $T_c =$ (a-b) 3500 K, (c-d) 2500 K, and (e-f) 1500 K.

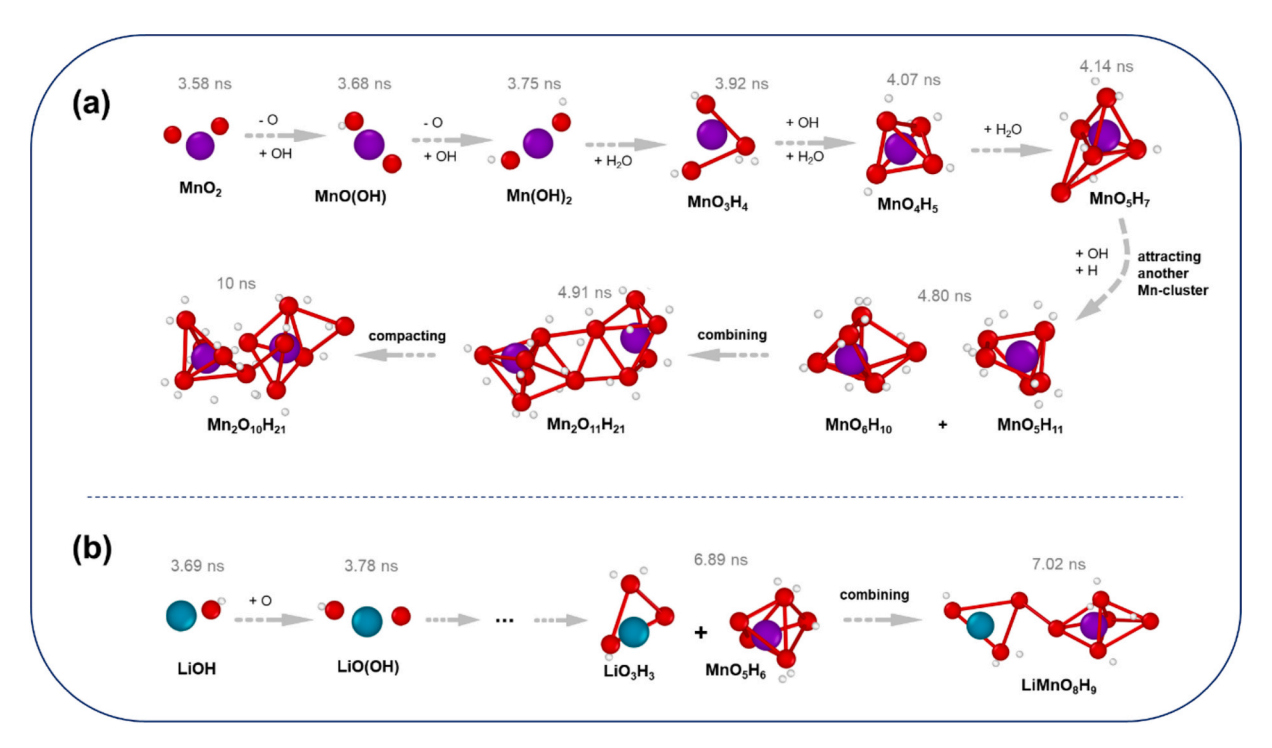


Fig. 11. Illustration of typical cluster formation pathways of (a) Mn-containing species and (b) Li-containing species during Stage III and IV.

 $T_c = 3500$ K, LiOH then primarily converts to Li(OH)₂ by adding an OH group (Fig. 12a), whereas at $T_c = 1500$ K both LiOH and LiO₂ decrease gradually without significant intermediate formation. After around 6.89 ns, LiO(OH) further oxidizes to LiO₃H₃. However, due to Li's lower valence and the limited number of Li atoms (only 40 in the simulation box), Li-containing species have difficulty forming stable fused crystal on their own at low temperature [86]. Instead, some Li species interact with Mn-containing cluster. For instance, LiO₃H₃ approaches a MnO₅H₆ cluster and eventually forms LiMnO₈H₉ at 7.02 ns (Fig. 11b). Other Licontaining species that do not interact with Mn clusters combine with carbon-hydrogen groups, leading to the formation of species such as $LiOCH_2$ and LiO_5CH_3 , as observed at all T_c values (Fig. 12b, d, and f). The crystal formation during nucleation in Stage III is primarily driven by the connection of Mn clusters, which are subsequently integrated with Li clusters. The influence of Mn-containing species on the crystallization of the Li-Mn-O phase has also been observed in experiments using X-ray diffraction [87].

Given the diversity of Li- and Mn-containing species in Stage III, it is

challenging to draw definitive conclusions about the influence of T_c solely from species concentrations. The evolution of the oxygen coordination number (CN) around Li and Mn atoms offers additional insights into the local atomic environments and structural changes over time. Fig. 13 shows the distribution of Li and Mn atoms with different CN values at $T_c = 2500$ K, where oxygen atoms within a 3.5 Å cutoff (based on prior studies) [88] define the first coordination shell. The shaded region in Fig. 13 corresponds to Stage III, during which significant CN changes are observed. For Li atoms, low CN values (1 and 2) drop markedly, while CN = 3 and 4 increase from 0 % to about 50 % and 30 %, respectively. For Mn atoms, over 80 % initially have CN = 2, but as oxidation proceeds, *CN* = 3 increases to roughly 70 %, followed by rapid increases in CN = 4 and CN = 5. By the end of Stage III, most Mn atoms exhibit CN = 5, with around 20 % reaching CN = 6. Fig. S11 presents similar CN trends for $T_c = 3500$ K, where Li atoms shift from primarily CN = 1 to a range of 2–4, and Mn atoms transition from CN = 1–2 to a range of 4–6. At $T_c = 1500$ K, the *CN* distributions differ slightly, with Li atoms mostly having CN values between 2 and 5, and Mn atoms

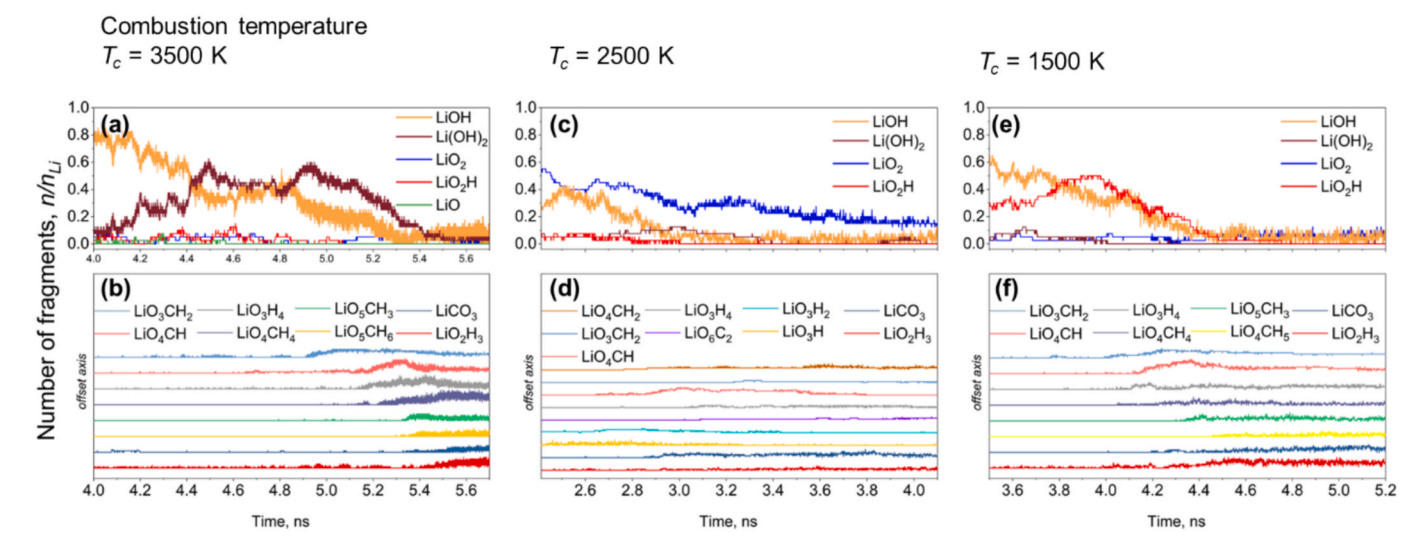


Fig. 12. Time evolution of the normalized number (n/n_{Li}) of Li-containing species throughout Stage III at combustion temperatures T_c = (a-b) 3500 K, (c-d) 2500 K, and (e-f) 1500 K.

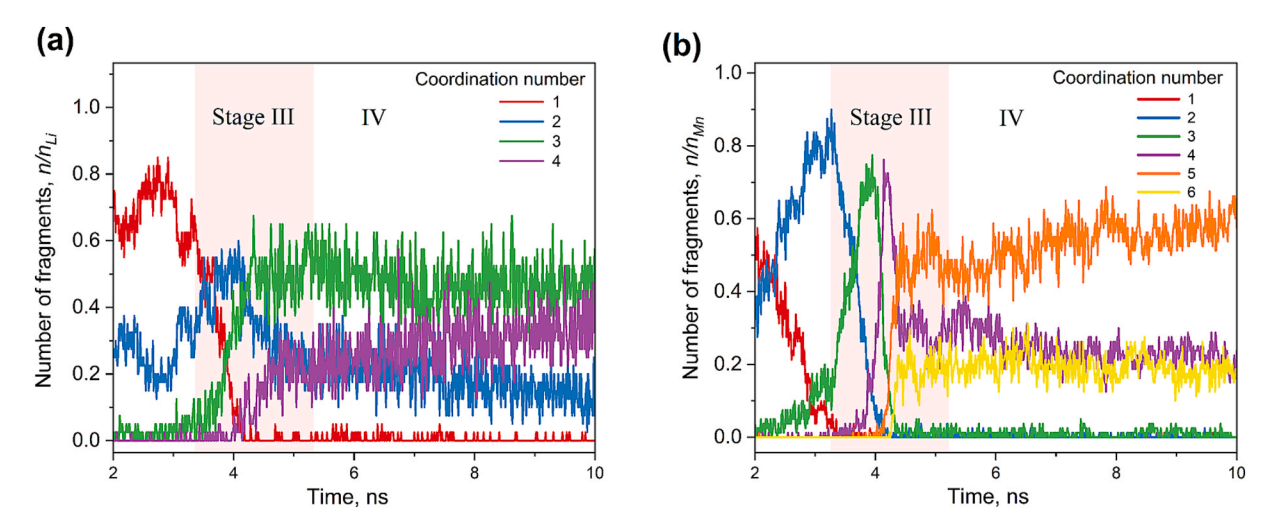


Fig. 13. Temporal evolution of (a) Li and (b) Mn atoms with different oxygen coordination number (CN) values at $T_c = 2500$ K. with Stage III shaded, during which significant CN changes are observed.

predominantly between 4 and 6.

Fig. 14 compares the evolution of CN for Li and Mn atoms at $T_c=1500$, 2500, and 3500 K. While the overall trends remain similar across different T_c , a noticeable time lag is observed at higher T_c due to the prolonged heating and cooling durations (Fig. 2). For Li, low CN values of 1 and 2 initially increase before dropping to nearly 0 %, while CN=3 and 4 become dominant in Stage III. Higher T_c conditions favor a larger fraction of Li atoms at CN=3, whereas lower T_c leads to a more pronounced presence of CN=4, which aligns with the LiO₄ tetrahedral structure [89] in spinel LiMn₂O₄ (illustrated in Fig. 13c). This trend is consistent with the product analysis in Fig. 12, suggesting that lower T_c enhances oxidation extent.

For Mn atoms, CN=1-3 decrease to 0 % by the end of Stage III. After Stage III, all T_c conditions yield similar fractions of Mn atoms with CN=4. However, $T_c=2500$ K exhibits the highest fraction of Mn atoms at CN=5, while both $T_c=3500$ K and $T_c=1500$ K show a higher fraction of Mn atoms with CN=6 compared to $T_c=2500$ K. This higher CN at $T_c=3500$ K can be attributed to the fact that, as discussed in Fig. 10, higher T_c promote the formation of more oxidized Mn species, whereas lower T_c lead to a greater degree of hydroxylation. Additionally, by examining the structure of the Mn clusters, it is found that more than half of the Mn

crystal structures become interconnected by O—O bonds by Stage IV, leading to an increase in Mn CN from 5 to 6, as illustrated by the snapshots in Fig. S13. In contrast, fewer Mn crystals connect at $T_c=2500$ K, and no connections are observed at $T_c=1500$ K. The increase in Mn atoms with CN=6 at $T_c=1500$ K during Stage IV can be attributed to the shorter combustion time (Fig. 2), which leaves excess oxygen for further oxidation (Fig. 9). However, the shorter combustion time also leads to incomplete oxidation of organic species, resulting in Mn- and Licontaining products that retain carbon contamination (Fig. S14), thereby inhibiting the formation of pure LiMn₂O₄.

In general, as shown in Fig. 13, Li atoms are predominantly found in III- or IV-fold coordination, with IV-fold coordination characteristic of ideal spinel LiMn₂O₄, where Li exists as LiO₄ tetrahedra [89]. Mn atoms are primarily found in IV- or VI-fold coordination, consistent with the LiMn₂O₄ structure, where Mn exists as MnO₆ [89]. Across all the T_c cases studied, both Li and Mn atoms are oxidized to varying extents, with some reaching the fully oxidized state corresponding to LiMn₂O₄. However, incomplete oxidation and carbon contamination at $T_c = 1500$ K suggest suboptimal crystal formation under these conditions. While the oxidation of Li does not show a strong dependence on high temperature, the minimal variation in Li coordination (with very close

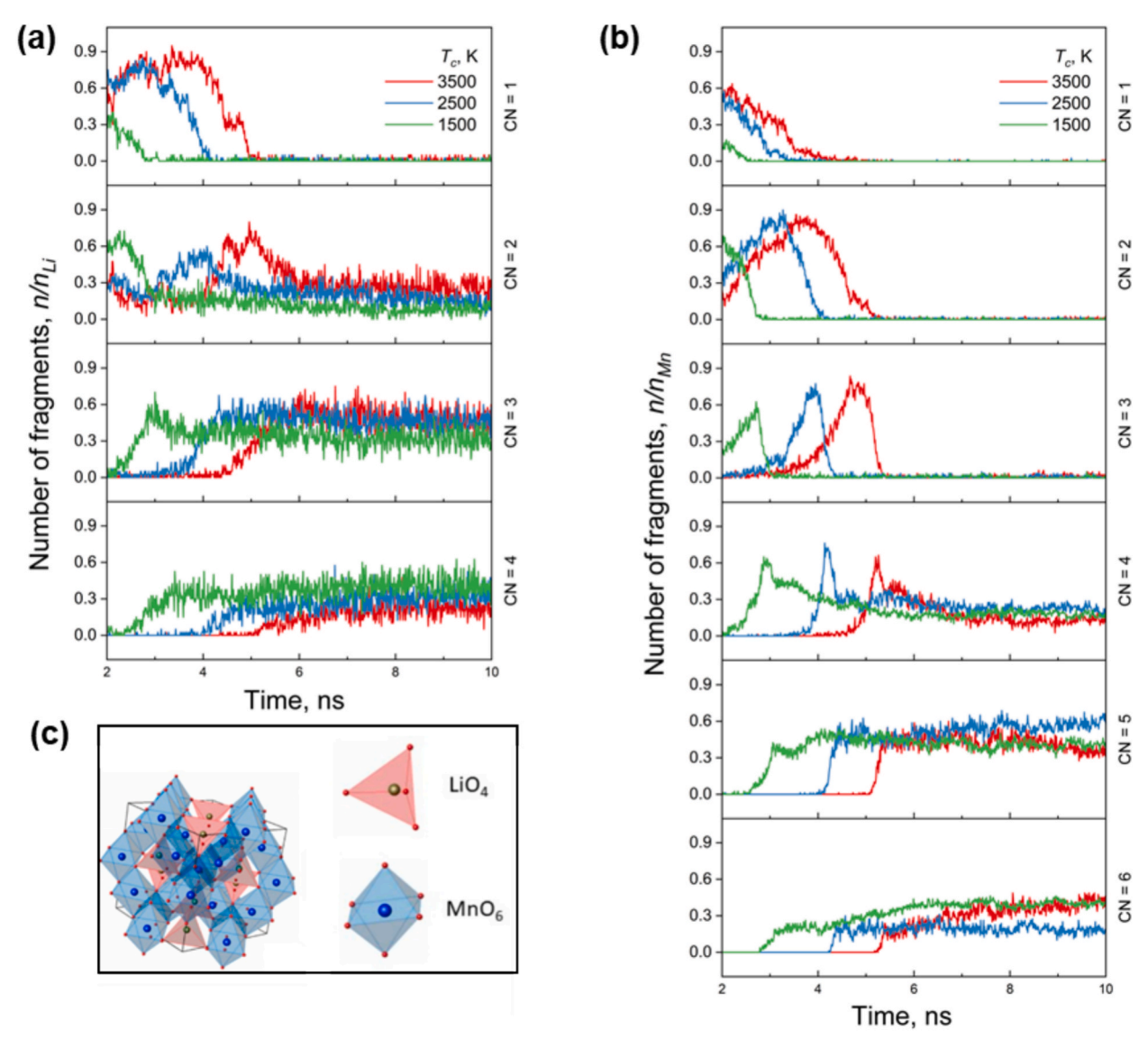


Fig. 14. Temporal evolution for different oxygen coordination number (CN) of (a) Li and (b) Mn atoms at $T_c = 1500$, 2500 and 3500 K. (c) Schematic representation of the spinel LiMn₂O₄ crystallographic structure, with LiO₄ tetrahedra and MnO₆ octahedron depicted.

fractions of CN=4 across all T_c cases) and the fact that the nucleation process is primarily driven by the aggregation of Mn clusters, followed by the integration of Li clusters, suggest that Mn plays a more dominant role in the nucleation process. Consequently, higher T_c conditions appear to be more favorable for forming LiMn₂O₄, as they promote enhanced crystal connectivity and more complete oxidation.

3.2.4. Stage IV: Particle growth by accretion and agglomeration

Fig. 15 presents the evolution of cluster size (a) in the largest cluster, (b) for the average of the five largest clusters for $T_c=1500$, 2500, and 3500 K. Based on Fig. 3a, Fig. S2a, and S4a, the system temperature at the onset of cluster growth is similar across cases, approximately 500–600 K. During the initial 1 ns of cluster growth, the largest clusters for all three T_c conditions exhibit comparable growth rates, as indicated by similar slopes in their growth curves (Fig. 15a). Likewise, the average cluster size increases at similar rates over the first 2 ns (Fig. 15b), suggesting that variations in the environmental species from prior reaction pathways have minimal influence on the cluster growth rate. At this early stage, the continuous growth of clusters points to accretion of small molecules as the dominant mechanism [39]. For example, at $T_c=2500$ K, snapshots in Fig. 15c show that from t = 4 to 6 ns, small clusters emerge from a well-mixed combustion product gas and grow uniformly

over time.

By t=7 ns, the clusters have grown significantly larger and the number of clusters in the simulation box is greatly reduced. The stepwise increases in both the largest and average cluster sizes indicate that, following initial accretion, growth proceeds primarily through the agglomeration of preformed clusters. Between t=7 and 8 ns (Fig. 15c), while some very large clusters are present, many small clusters remain. Over time, the larger clusters gradually incorporate these smaller ones. By t=10 ns, only a few large clusters remain, with almost no small clusters existing. Snapshots for $T_c=1500$ K and $T_c=3500$ K (Figs. S15 and S16) reveal that the overall evolution of the system is similar despite differences in combustion temperature.

Comparing the growth profiles across different T_c values (Fig. 14a), clusters at $T_c=2500$ and 3500 K exhibit nearly identical growth behavior. In contrast, although growth is slower at $T_c=1500$ K initially, a significant surge in growth occurs near the end of the simulation, leading to the largest clusters overall. This behavior likely arises from the longer time available for the accumulation and agglomeration of clusters at lower temperatures. It is reasonable to anticipate that, given a longer simulation time, clusters at $T_c=2500$ and 3500 K would experience a similar late-stage growth surge. This observation highlights the importance of timely particle collection in FSP to prevent unwanted

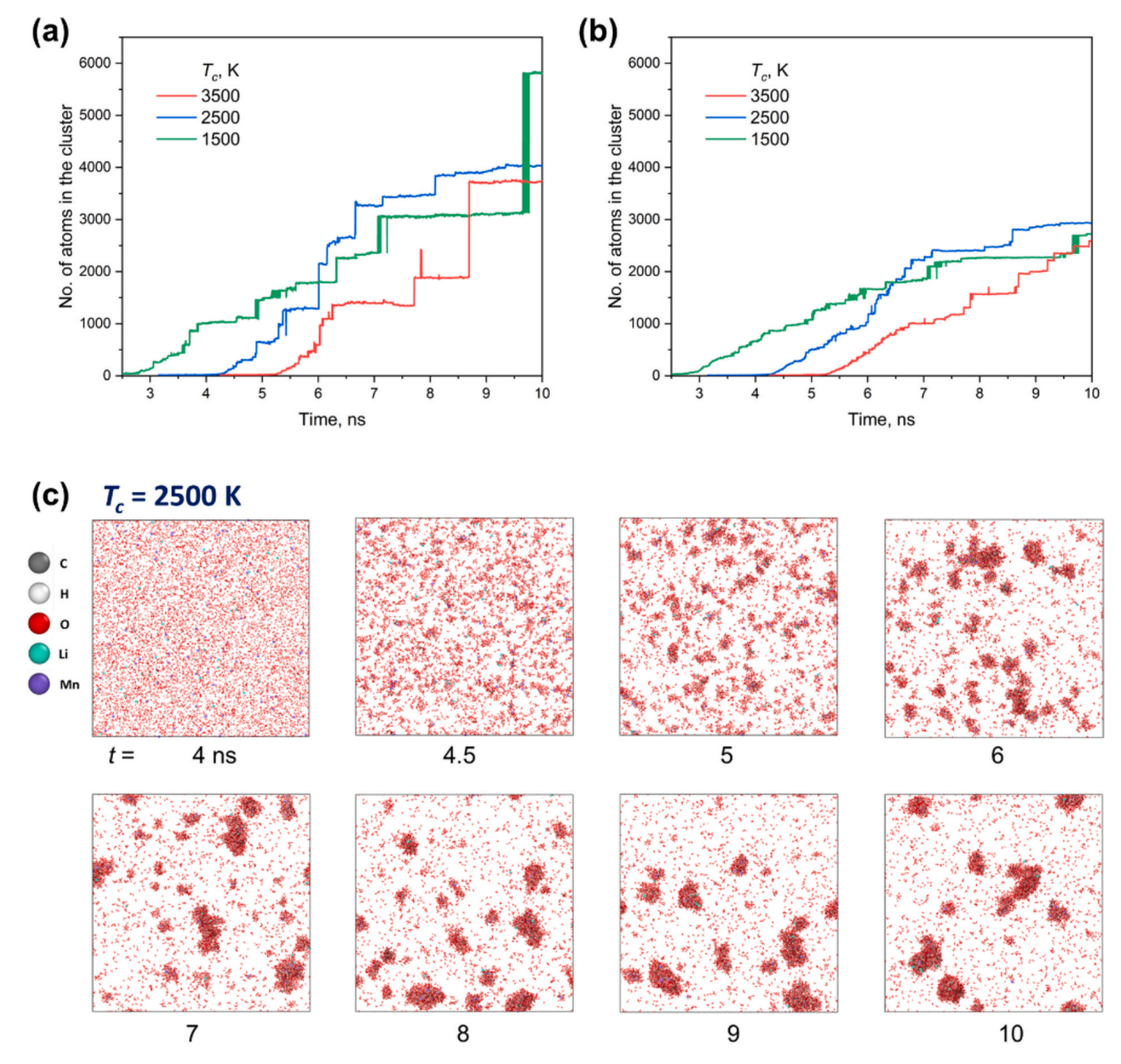


Fig. 15. Evolution of (a) the number of atoms in the largest cluster and (b) the average number of atoms in the five largest clusters for $T_c = 1500$, 2500, and 3500 K. (c) Snapshots of the simulation system during t = 4-10 ns at $T_c = 2500$ K.

agglomeration, as previous experiments have shown that prolonged agglomeration at room temperature can result in permanent aggregation [90].

To examine the formed cluster in more detail, Fig. 16 shows the evolution of the largest cluster at $T_c = 2500$ K from t = 5.5 ns to t = 10 ns. Initially, the cluster is composed primarily of a carbon-oxygen framework formed by unoxidized organic species. Over time, oxidized Li- and Mn-containing species are progressively incorporated into the structure. By t = 10 ns, the largest cluster comprises 5Li atoms, 13 Mn atoms, and a substantial CHO backbone. From the structure of the cluster, we could find that the cluster growth is more by weakly bonded soft agglomerations from organic framework rather than by the strongly bonded metal crystal bonds. This occurs because, as the temperature decreases downstream in the flame, sintering is suppressed, and particle interactions are restricted to the formation of weakly bonded soft agglomerates [91]. The presence of organic impurities aligns with experimental observations, where SEM-EDS analysis revealed a uniform distribution of carbon, oxygen, and manganese in the particles produced after FSP [92].

4. Post-synthesis refinement by annealing

The analysis above demonstrated that formation of large clusters during cooling is driven by the accretion and agglomeration of combustion products. However, experimental studies suggest that further refinements such as annealing are necessary to remove the impurity and to develop the final crystal structure [29,32]. During annealing, clusters react with a continuous gas flow that removes evaporated oxidized nonmetal species [17,29,32].

To simulate this process, we annealed the largest cluster at 1000 K [17] for 0.02 ns in the presence of 250 additional O_2 molecules. After cooling, the resulting cluster was transferred into fresh O_2 gas, and the annealing cycle was repeated to mimic the continuous introduction of fresh gases as in experiments. After four annealing cycles, more than 43 % of the non-metallic atoms were reduced, indicating that iterative annealing could eventually remove most non-metallic species, leaving predominantly metal oxides.

To further simulate conditions where the cluster is sufficiently annealed (after enough rounds of simulated annealing), Li and Mn atoms—with their coordinated oxygen—were extracted and annealed in

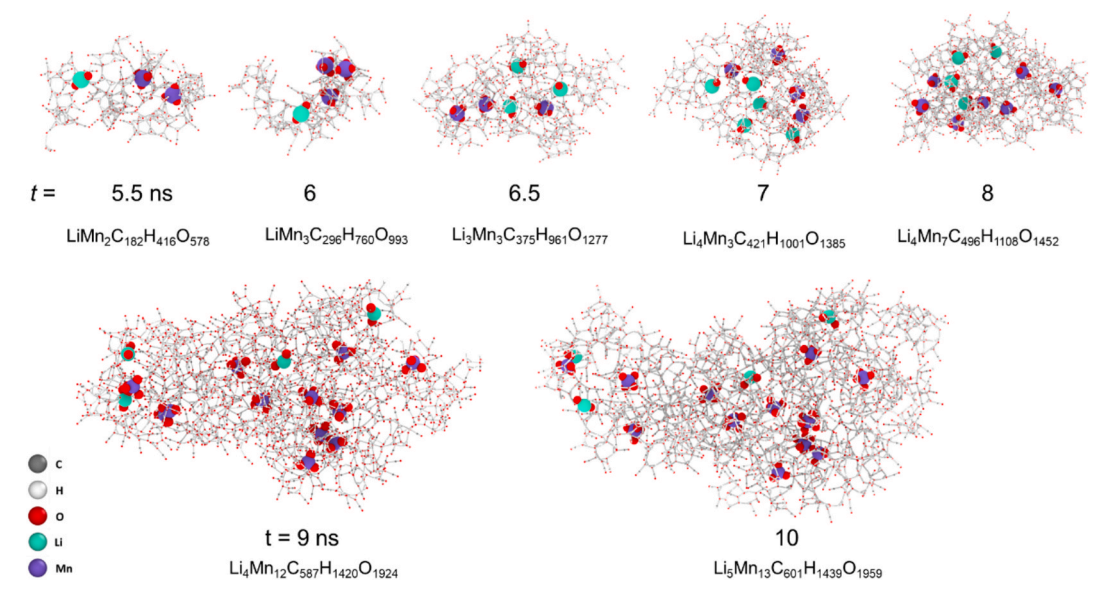


Fig. 16. Snapshots of the largest cluster in the simulation box during t = 5.5-10 ns (Stages IV) at $T_c = 2500$ K. The images illustrate the cluster growth process and internal structure, with C—C bonds highlighted to emphasize the organic framework and magnified views of Li and Mn atoms provided for clearer visualization.

an NPT ensemble at 1 atm. This process ultimately resulted in the formation of a final crystal structure, as shown in Fig. 17. Although the overall cluster remains largely amorphous, certain local regions (as indicated by the boxed MnO_6 octahedron structure) exhibit localized formation of $LiMn_2O_4$ crystals, closely resembling the ideal spinel structure. Polycrystalline particles with locally amorphous structures have also been observed in experiments through TEM imaging [92].

5. Conclusion

This study developed a ReaxFF molecular dynamics model to simulate key atomic-scale processes during the flame spray pyrolysis (FSP) synthesis of $LiMn_2O_4$, providing detailed insights into reaction pathways and particle formation mechanisms, from precursor droplet evaporation to post-combustion annealing. The FSP mechanism was divided into four stages: evaporation and initial decomposition, combustion-driven

oxidation, nucleation, and particle growth through accretion and agglomeration, which were consistent with experimental observations. Simulations at combustion temperatures (T_c) ranging from 1500 to 3500 K revealed temperature-dependent reaction pathways and structural evolution. The key findings are summarized as follows:

Evaporation & Initial Decomposition: The evaporation of precursor droplet is accompanied by exothermic oxidation. The Licontaining precursors decompose fully and have a faster diffusion facilitated by lower valence and atomic mass, while Mn-containing species retain C_5 groups through complex decomposition pathways, ultimately achieving uniform diffusion.

Combustion-Driven Oxidation: Intense combustion results in rapid oxygen consumption. Li-containing species, primarily LiO_2 from Stage I, convert to LiOH through OH radical reactions, with higher T_c accelerating this transition (over 80 % at 3500 K compared to \sim 50 %

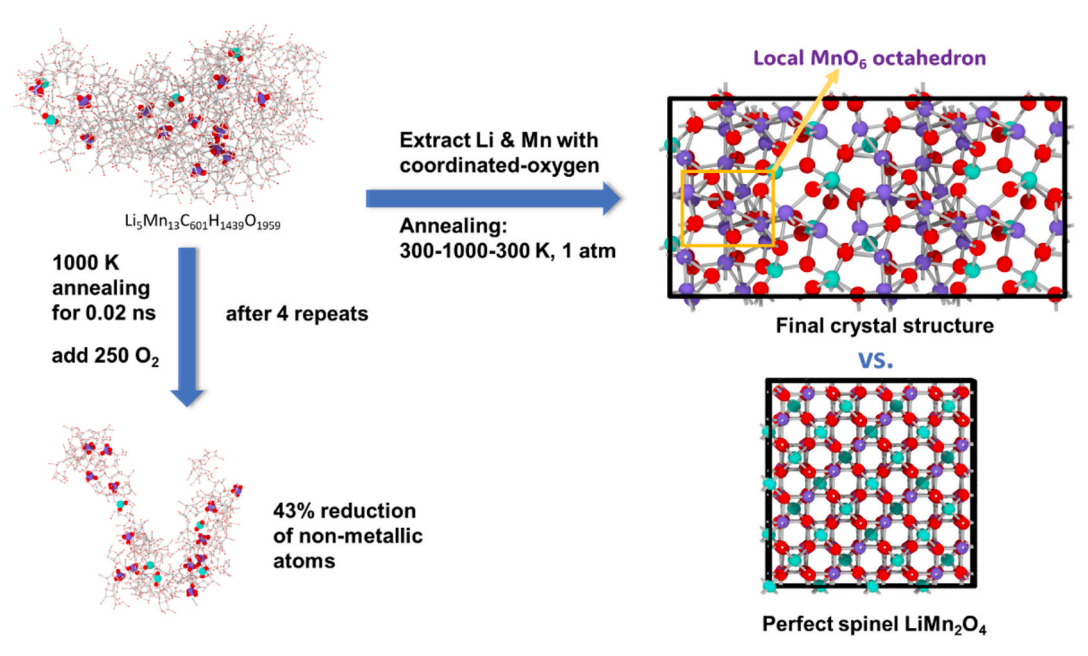


Fig. 17. Illustration of simulated annealing process and the final crystal structure, with perfect spinel LiMn₂O₄ crystal box shown.

at 1500 K). Other intermediates such as LiO_2H and $\text{Li}(\text{OH})_2$ also contribute. Mn-containing species exhibit greater temperature sensitivity. At $T_c > 1500$ K, oxidation proceeds via dehydroxylation and dehydrogenation of MnC₅ intermediates, forming MnO₂ and MnO₂H. At lower T_c (1500 K), slower reaction kinetics stabilizes hydroxylated species like Mn(OH)₂ and MnO₃H₄. T_c plays a crucial role in restructuring Mn reaction pathways, while primarily modulating the decomposition extent for Li species.

Nucleation: Nucleation is accompanied by continuous oxidation, with Li and Mn undergoing varying oxidation degrees and some reaching full coordination, corresponding to the LiMn2O4 crystal structure. Mn-containing species follow temperature-dependent oxidation and hydroxylation pathways, leading to the formation of $Mn_xO_vH_z$ (x, y, z > 0) through Mn—O and O—O bond reorganization, ultimately forming connected crystal clusters. Li-containing species integrate into Mn clusters or organic fragments, showing that nucleation is primarily Mn-driven and is more favorable at higher T_c . Particle Growth: Clusters grow initially through molecular accretion at similar rates across all T_c values, later transitioning to cluster agglomeration. At $T_c = 1500$ K, late-stage agglomeration is observed due to prolonged accumulation. The clusters consist primarily of carbon-oxygen frameworks, incorporating Li- and Mn-containing species through weak organic interactions, rather than forming crystalline metal bonds. This reflects suppressed sintering at lower temperatures and highlights the importance of timely particle collection in FSP to prevent excessive agglomeration.

The post-synthesis refinement process, simulated through iterative annealing, showed that continuous oxidative annealing can remove non-metallic species and drive structural reorganization, resulting in predominantly Li/Mn-oxides with localized crystallization into LiMn $_2$ O $_4$ spinel domains. These findings align with experimental TEM observations, demonstrating the transition from amorphous agglomerates to functional crystalline materials.

Throughout the FSP process, Li and Mn play distinct roles due to their intrinsic properties and decomposition/oxidation pathways. Li, with its lower atomic mass and valence, is a mobile and reactive participant, undergoing rapid decomposition, promoting evaporation, and aiding diffusion. In contrast, Mn, with its higher valence and complex bonding dynamics, follows temperature-sensitive reaction pathways that favor high-temperature combustion, leading to fully oxidized products. Mn plays a central role in nucleation by forming a crystal framework, while Li remains incorporated into it. Combustion temperature critically governs reaction kinetics, intermediate stability, and product composition during FSP. Higher T_c (>1500 K) intensifies oxidation, accelerating O2 consumption, and promoting thermodynamically favored pathways for both Li- and Mn-containing species. Lower T_c (1500 K) slows reaction rates, favoring hydroxylated species and resulting in incomplete decomposition. Notably, T_c modulates Mn's role as the structural architect: higher T_c enhances Mn-driven oxide crystallization and crystal fusion, while lower T_c traps Mn in hydroxylated, amorphous frameworks.

While partial oxidation and the formation of target coordination environments for both Li and Mn atoms are evident, oxygen limitation in the system restricts the full transformation to LiMn $_2$ O $_4$. Future studies should explore varying oxygen equivalence ratios or extended combustion time to optimize oxidation and achieve a higher yield of the desired product.

This work bridges atomic-scale FSP dynamics with nanomaterial production in experiments, highlighting the interplay between combustion conditions, elemental chemistry, and post-processing in tailoring crystallinity. The computational framework provides a valuable tool for understanding and optimizing the FSP process to achieve the desired composition, size, crystallinity, and ultimately, performance in lithium-ion batteries.

Funding statement

The research is supported by the Carbon Neutrality and Energy System Transformation (CNEST) Program led by Tsinghua University. Funding from the UK Engineering and Physical Sciences Research Council under Grant Nos. EP/T015233/1 and EP/X035875/1) is also acknowledged. This work made use of computational support by CoSeC, the Computational Science Centre for Research Communities, through UKCOMES.

CRediT authorship contribution statement

Yi Wang: Writing – review & editing, Writing – original draft, Visualization, Software, Methodology, Investigation, Formal analysis, Data curation, Conceptualization. Muye Feng: Writing – review & editing, Validation, Software, Methodology, Investigation. Dingyu Hou: Writing – review & editing, Validation, Methodology, Investigation. Ruitian He: Writing – review & editing, Validation, Methodology, Conceptualization. Kai Hong Luo: Writing – review & editing, Supervision, Resources, Project administration, Investigation, Funding acquisition, Conceptualization.

Declaration of competing interest

The authors declare that they have no known competing financial interests or personal relationships that could have appeared to influence the work reported in this paper.

Appendix A. Supplementary data

Fig. S1–S16 and Table S1–S2 provide detailed information on simulation setup, temporal evolution of oxygen, system temperature, and reaction stages at different combustion temperatures. Snapshots illustrate precursor evaporation, atomic diffusion, and reaction pathways while time evolution data track Li- and Mn-containing species, oxygen coordination number analysis, and reaction network. Structural visualizations depict the Li and Mn coordination environments and nanoparticle growth at various stages.

Supplementary data to this article can be found online at https://doi.org/10.1016/j.cej.2025.163073.

Data availability

Data will be made available on request.

References

- J.M. Tarascon, M. Armand, Issues and challenges facing rechargeable lithium batteries, Nature 414 (2001) 359–367, https://doi.org/10.1038/35104644.
- [2] J.B. Goodenough, K.S. Park, The Li-Ion Rechargeable Battery: A Perspective, JACS 135 (2013) 1167–1176, https://doi.org/10.1021/ja3091438.
- [3] W.G. Howard, C.L. Schmidt, E.R. Scott, Medical device having lithium-ion battery, Google Patents (2008).
- [4] H. Zeng, B. Xing, C. Zhang, L. Chen, H. Zhao, X. Han, G. Yi, G. Huang, C. Zhang, Y. Cao, In Situ Synthesis of MnO₂/Porous Graphitic Carbon Composites as High-Capacity Anode Materials for Lithium-Ion Batteries, Energy Fuels 34 (2020) 2480–2491, https://doi.org/10.1021/acs.energyfuels.9b04325.
- [5] H. Xu, L. Zhao, X. Liu, Q. Huang, Y. Wang, C. Hou, Y. Hou, J. Wang, F. Dang, J. Zhang, Metal-Organic-Framework Derived Core-Shell N-Doped Carbon Nanocages Embedded with Cobalt Nanoparticles as High-Performance Anode Materials for Lithium-Ion Batteries, Adv. Funct. Mater. 30 (2020) 2006188, https://doi.org/10.1002/adfm.202006188.
- [6] Z. Iskandar Radzi, K. Helmy Arifin, M. Zieauddin Kufian, V. Balakrishnan, S. Rohani Sheikh Raihan, N. Abd Rahim, R. Subramaniam, Review of spinel LiMn₂O₄ cathode materials under high cut-off voltage in lithium-ion batteries: Challenges and strategies, J. Electroanal. Chem. 920 (2022) 116623, https://doi. org/10.1016/j.jelechem.2022.116623.
- [7] D. Miranda, A.M. Almeida, S. Lanceros-Méndez, C.M. Costa, Effect of the active material type and battery geometry on the thermal behavior of lithium-ion batteries, Energy 185 (2019) 1250–1262, https://doi.org/10.1016/j. energy.2019.07.099.

- [8] M. Loganathan, B. Mishra, C.M. Tan, T. Kongsvik, R. Rai, Multi-Criteria decision making (MCDM) for the selection of Li-Ion batteries used in electric vehicles (EVs), Mater. Today Proc. 41 (2021) 1073–1077, https://doi.org/10.1016/j. mater. 2020.07.179
- [9] T. Prasankumar, J. Vigneshwaran, M. Bagavathi, S. Jose, Expeditious and ecofriendly synthesis of spinel LiMnO and its potential for fabrication of supercapacitors, J. Alloys Compd. 834 (2020) 155060, https://doi.org/10.1016/j. jallcom.2020.155060.
- [10] H. Li, C. Erinmwingbovo, J. Birkenstock, M. Schowalter, A. Rosenauer, F. La Mantia, L. M\u00e4dler, S. Pokhrel, Double Flame-Fabricated High-Performance AlPO4/ LiMn₂O₄ Cathode Material for Li-Ion Batteries, ACS Appl. Energy Mater. 4 (2021) 4428-4443, https://doi.org/10.1021/acsaem.1c00024.
- [11] T. Erichsen, B. Pfeiffer, V. Roddatis, C.A. Volkert, Tracking the Diffusion-Controlled Lithiation Reaction of LiMn₂O₄ by In Situ TEM, ACS Appl. Energy Mater. 3 (2020) 5405–5414, https://doi.org/10.1021/acsaem.0c00380.
- [12] Y. Wu, Z. Wen, H. Feng, J. Li, Hollow Porous LiMn₂O₄ Microcubes as Rechargeable Lithium Battery Cathode with High Electrochemical Performance, Small 8 (2012) 858–862, https://doi.org/10.1002/smll.201101838.
- [13] E. Rada, E. Lima, F. Ruiz, M. Sergio Moreno, Synthesis of LiMn₂O₄ nanostructures with controlled morphology, MSEB 292 (2023) 116410, https://doi.org/10.1016/ i.msch.2023.116410
- [14] J.M. Paulsen, J.R. Dahn, Phase Diagram of LiMnO Spinel in Air, Chem. Mater. 11 (1999) 3065–3079, https://doi.org/10.1021/cm9900960.
- [15] H. Xia, Z. Luo, J. Xie, Nanostructured LiMn₂O₄ and their composites as high-performance cathodes for lithium-ion batteries, Prog. Nat. Sci.: Mater. Int. 22 (2012) 572–584, https://doi.org/10.1016/j.pnsc.2012.11.014.
- [16] S. Martinet, Nanomaterials for Rechargeable Lithium Batteries, Angew. Chem. Int. Ed. (2016) 2930–2946, https://doi.org/10.1002/anie.200702505.
- [17] F.O. Ernst, H.K. Kammler, A. Roessler, S.E. Pratsinis, W.J. Stark, J. Ufheil, P. Novák, Electrochemically active flame-made nanosized spinels: LiMn₂O₄, Li₄Ti₅O₁₂ and LiFe₅O₈, Mater. Chem. Phys. 101 (2007) 372–378, https://doi.org/ 10.1016/j.matchemphys.2006.06.014.
- [18] Y. Chen, K. Xie, Y. Pan, C. Zheng, Nano-sized LiMn₂O₄ spinel cathode materials exhibiting high rate discharge capability for lithium-ion batteries, J. Power Sources 196 (2011) 6493–6497, https://doi.org/10.1016/j.jpowsour.2011.03.081.
- [19] G. Arnold, J. Garche, R. Hemmer, S. Ströbele, C. Vogler, M. Wohlfahrt-Mehrens, Fine-particle lithium iron phosphate LiFePO₄ synthesized by a new low-cost aqueous precipitation technique, J. Power Sources 119–121 (2003) 247–251, https://doi.org/10.1016/S0378-7753(03)00241-6.
- [20] B. Buesser, S.E. Pratsinis, Design of nanomaterial synthesis by aerosol processes, Annu. Rev. Chem. Biomol. Eng. 3 (2012) 103–127, https://doi.org/10.1146/ annurev-chembioeng-062011-080930.
- [21] G.A. Kelesidis, S.E. Pratsinis, A perspective on gas-phase synthesis of nanomaterials: Process design, impact and outlook, Chem. Eng. J. 421 (2021) 129884, https://doi.org/10.1016/j.cej.2021.129884.
 [22] G.A. Kelesidis, E. Goudeli, S.E. Pratsinis, Flame synthesis of functional
- [22] G.A. Kelesidis, E. Goudeli, S.E. Pratsinis, Flame synthesis of functional nanostructured materials and devices: Surface growth and aggregation, Proc. Combust. Inst. 36 (2017) 29–50, https://doi.org/10.1016/j.proci.2016.08.078.
 [23] T.J. Patey, R. Büchel, S.H. Ng, F. Krumeich, S.E. Pratsinis, P. Novák, Flame co-
- [23] T.J. Patey, R. Büchel, S.H. Ng, F. Krumeich, S.E. Pratsinis, P. Novák, Flame cosynthesis of LiMn O and carbon nanocomposites for high power batteries, J. Power Sources 189 (2009) 149–154, https://doi.org/10.1016/j.jpowsour.2008.10.002.
- [24] S. Pokhrel, L. M\u00e4dler, Flame-made Particles for Sensors, Catalysis, and Energy Storage Applications, Energy Fuels 34 (2020) 13209–13224, https://doi.org/ 10.1021/acs.energyfuels.0c02220.
- [25] L. Singh, A. Kumar, H. Lee, J. Lee, M. Ji, Y. Lee, Ultrafast auto flame synthesis for the mass production of LiCoO as a cathode material for Li-ion batteries, J. Solid State Electrochem 22 (2018) 2561–2568, https://doi.org/10.1007/s10008-018-3972-5
- [26] M. Konarova, I. Taniguchi, Preparation of carbon coated LiFePO by a combination of spray pyrolysis with planetary ball-milling followed by heat treatment and their electrochemical properties, Powder Technol. 191 (2009) 111–116, https://doi. org/10.1016/j.powtec.2008.09.013.
- [27] L. Singh, J. Lee, G.W. Kim, M. Ji, C. Moon, H. Lee, J.W. Ha, Y. Lee, A simple, rapid and efficient flame synthesis of ultrafine LiNiCoTiO(=0.25 and 0.30): a versatile route to synthesize Ni-rich cathode materials for Li-ion batteries, NJC 42 (2018) 372–379, https://doi.org/10.1039/c7nj02679j.
- [28] J.H. Yi, J.H. Kim, H.Y. Koo, Y.N. Ko, Y.C. Kang, J.-H. Lee, Nanosized LiMn₂O₄ powders prepared by flame spray pyrolysis from aqueous solution, J. Power Sources 196 (2011) 2858–2862, https://doi.org/10.1016/j.jpowsour.2010.11.038.
- [29] X. Zhang, H. Zheng, V. Battaglia, R.L. Axelbaum, Electrochemical performance of spinel LiMn₂O₄ cathode materials made by flame-assisted spray technology, J. Power Sources 196 (2011) 3640–3645, https://doi.org/10.1016/j. jpowsour.2010.07.008.
- [30] T.J. Patey, R. Büchel, M. Nakayama, P. Novák, Electrochemistry of LiMn₂O₄ nanoparticles made by flame spray pyrolysis, PCCP 11 (2009) 3756–3761, https://doi.org/10.1039/B821572N.
- [31] T.J. Patey, R. Büchel, S.H. Ng, F. Krumeich, S.E. Pratsinis, P. Novák, Flame cosynthesis of LiMn₂O₄ and carbon nanocomposites for high power batteries, J. Comput. Phys. J. Power Sources 189 (2009) 149–154, https://doi.org/10.1016/j.jpowsour.2008.10.002.
- [32] S.Y. Chew, T.J. Patey, O. Waser, S.H. Ng, R. Büchel, A. Tricoli, F. Krumeich, J. Wang, H.K. Liu, S.E. Pratsinis, P. Novák, Thin nanostructured $LiMn_2O_4$ films by flame spray deposition and in situ annealing method, J. Power Sources 189 (2009) 449–453, https://doi.org/10.1016/j.jpowsour.2008.12.085.
- [33] T.P. Senftle, S. Hong, M.M. Islam, S.B. Kylasa, Y. Zheng, Y.K. Shin, C. Junkermeier, R. Engel-Herbert, M.J. Janik, H.M. Aktulga, T. Verstraelen, A. Grama, A.C.T. van

- Duin, The ReaxFF reactive force-field: development, applications and future directions, Npj Comput. Mater. 2 (2016) 15011, https://doi.org/10.1038/npjcompumats.2015.11.
- [34] S. Jeong, D. Bresser, D. Buchholz, M. Winter, S. Passerini, Carbon coated lithium sulfide particles for lithium battery cathodes, J. Power Sources 235 (2013) 220–225, https://doi.org/10.1016/j.jpowsour.2013.01.084.
- [35] S. Tajimi, Y. Ikeda, K. Uematsu, K. Toda, M. Sato, Enhanced electrochemical performance of LiFePO prepared by hydrothermal reaction, Solid State Ion. 175 (2004) 287–290, https://doi.org/10.1016/j.ssi.2003.12.033.
- [36] X.J. Wang, Y.Y. Hou, Y.S. Zhu, Y.P. Wu, R. Holze, An Aqueous Rechargeable Lithium Battery Using Coated Li Metal as Anode, Sci. Rep. 3 (2013) 1401, https://doi.org/10.1038/srep01401.
- [37] L. M\u00e4dler, H.K. Kammler, R. Mueller, S.E. Pratsinis, Controlled synthesis of nanostructured particles by flame spray pyrolysis, J. Aerosol Sci. 33 (2002) 369–389. https://doi.org/10.1016/S0021-8502(01)00159-8.
- [38] C. Sun, A.X. Zhu, R.K. Wang, H.X. Liu, Pyrolysis reaction mechanisms and chlorine migration of tetrachlorobiphenyl a through the integration of ReaxFF-MD and DFT, J. Environ. Chem. Eng. 12 (2024) 112778, https://doi.org/10.1016/j. jece.2024.112778.
- [39] Y. Wang, E. Goudeli, The onset of aerosol Au nanoparticle crystallization: accretion & explosive nucleation, Nanoscale 16 (2024) 17942–17953, https://doi.org/ 10.1039/D4NR02359E.
- [40] D. Hou, L. Pascazio, J. Martin, Y. Zhou, M. Kraft, X. You, On the reactive coagulation of incipient soot nanoparticles, J. Aerosol Sci. 159 (2022) 105866, https://doi.org/10.1016/j.jaerosci.2021.105866.
- [41] Q. Mao, Y. Ren, K.H. Luo, S. Li, Sintering-Induced Phase Transformation of Nanoparticles: A Molecular Dynamics Study, J. Phys. Chem. C 119 (2015) 28631–28639, https://doi.org/10.1021/acs.jpcc.5b08625.
- [42] J. Wei, A. Ostadhossein, S. Li, M. Ihme, Kinetics for the hydrolysis of Ti(OC₃H₇)₄: A molecular dynamics simulation study, Proc. Combust. Inst. 38 (2021) 1433–1440, https://doi.org/10.1016/j.proci.2020.06.345.
- [43] D. Hou, M. Feng, J. Wei, Y. Wang, A.C.T. van Duin, K.H. Luo, A reactive force field molecular dynamics study on the inception mechanism of titanium tetraisopropoxide (TTIP) conversion to titanium clusters, Chem. Eng. Sci. 252 (2022) 117496, https://doi.org/10.1016/j.ces.2022.117496.
- [44] S. Reddivari, C. Lastoskie, R. Wu, J. Zhang, Chemical composition and formation mechanisms in the cathode-electrolyte interface layer of lithium manganese oxide batteries from reactive force field (ReaxFF) based molecular dynamics, Front. Energy Res. 11 (2017) 365–373, https://doi.org/10.1007/s11708-017-0500-8.
- [45] M.K. Talkhoncheh, H. Ghods, M. Doosthosseini, J. Silberberg, I. Kyprianou, A.C. T. van Duin, Development of the ReaxFF Reactive Force Field for Li/Mn/O Battery Technology with Application to Design a Self-Healing Cathode Electrolyte Interphase, J. Phys. Chem. C 128 (2024) 6538–6550, https://doi.org/10.1021/acs.ipcc.3c07242.
- [46] M. Feng, H. Li, K.H. Luo, A molecular dynamics study on oxidation of aluminum hydride (AlH3)/hydroxyl-terminated polybutadiene (HTPB) solid fuel, Proc. Combust. Inst. 38 (2021) 4469–4476, https://doi.org/10.1016/j. proci 2020.09.023
- [47] K. Chenoweth, A.C.T. van Duin, W.A. Goddard, ReaxFF reactive force Field for molecular dynamics simulations of hydrocarbon oxidation, J. Phys. Chem. A 112 (2008) 1040–1053, https://doi.org/10.1021/jp709896w.
- [48] Q. Mao, A.C.T. van Duin, K.H. Luo, Investigation of methane oxidation by palladium-based catalyst via ReaxFF Molecular Dynamics simulation, Proc. Combust. Inst. 36 (2017) 4339–4346, https://doi.org/10.1016/j. procj. 2016.08.037
- [49] S. Bhoi, T. Banerjee, K. Mohanty, Molecular dynamic simulation of spontaneous combustion and pyrolysis of brown coal using ReaxFF, Fuel 136 (2014) 326–333, https://doi.org/10.1016/j.fuel.2014.07.058.
- [50] F. Guo, X. Cheng, H. Zhang, ReaxFF Molecular Dynamics Study of Initial Mechanism of JP-10 Combustion, Combust. Sci. Technol. 184 (2012) 1233–1243, https://doi.org/10.1080/00102202.2012.679714.
- [51] W.A. Goddard, A. van Duin, K. Chenoweth, M.-J. Cheng, S. Pudar, J. Oxgaard, B. Merinov, Y.H. Jang, P. Persson, Development of the ReaxFF reactive force field for mechanistic studies of catalytic selective oxidation processes on BiMoOx, Top. Catal. 38 (2006) 93, https://doi.org/10.1007/s11244-006-0074-x.
- [52] C. Zou, Y.K. Shin, A.C.T. van Duin, H. Fang, Z. Liu, Molecular dynamics simulations of the effects of vacancies on nickel self-diffusion, oxygen diffusion and oxidation initiation in nickel, using the ReaxFF reactive force field, Acta Mater. 83 (2015) 102–112, https://doi.org/10.1016/j.actamat.2014.09.047.
- [53] M.Y. Sengul, C.A. Randall, A.C.T. van Duin, ReaxFF Molecular Dynamics Study on the Influence of Temperature on Adsorption, Desorption, and Decomposition at the Acetic Acid/Water/ZnO(101⁻0) Interface Enabling Cold Sintering, ACS Appl. Mater. Interfaces 10 (2018) 37717–37724, https://doi.org/10.1021/
- [54] L. Zhang, Y. Lu, M. Rostam Abadi, Sintering of calcium oxide (CaO) during CO₂ chemisorption: a reactive molecular dynamics study, PCCP 14 (2012) 16633–16643, https://doi.org/10.1039/C2CP42209C.
- [55] A. Strachan, A.C.T. van Duin, D. Chakraborty, S. Dasgupta, W.A. Goddard, Shock Waves in High-Energy Materials: The Initial Chemical Events in Nitramine RDX, PRL 91 (2003) 098301, https://doi.org/10.1103/PhysRevLett.91.098301.
- [56] L. Zhang, S.V. Zybin, A.C.T.v. Duin, S. Dasgupta, W.A. Goddard III, Thermal Decomposition of Energetic Materials by ReaxFF Reactive Molecular Dynamics, AIP Conference Proceedings 845 (2006) 589–592, https://doi.org/10.1063/ 1.2263391.

- [57] T. Zhou, H. Song, Y. Liu, F. Huang, Shock initiated thermal and chemical responses of HMX crystal from ReaxFF molecular dynamics simulation, PCCP 16 (2014) 13914–13931, https://doi.org/10.1039/C4CP00890A.
- [58] S. Plimpton, Fast parallel algorithms for short-range molecular dynamics, J. Comput. Phys. 117 (1995) 1–19, https://doi.org/10.1006/jcph.1995.1039.
- [59] A.K. Rappe, W.A. Goddard III, Charge equilibration for molecular dynamics simulations, J. Phys. Chem. 95 (1991) 3358–3363.
- [60] S. Reddivari, Electrode-electrolyte interface layers in lithium ion batteries using reactive force field based molecular dynamics, University of Michigan, 2016.
- [61] S.S. Han, A.C.T. van Duin, W.A. Goddard, H.M. Lee, Optimization and Application of Lithium Parameters for the Reactive Force Field, ReaxFF, J. Phys. Chem. A 109 (2005) 4575–4582, https://doi.org/10.1021/jp051450m.
- [62] G. Zhou, X. Sun, Q.H. Li, X. Wang, J. Zhang, W. Yang, X. Yu, R. Xiao, H. Li, Mn Ion Dissolution Mechanism for Lithium-Ion Battery with LiMn₂O₄ Cathode: In Situ Ultraviolet–Visible Spectroscopy and Ab Initio Molecular Dynamics Simulations, J. Phys. Chem. Lett. 11 (2020) 3051–3057, https://doi.org/10.1021/acs. inclett 0c0036
- [63] T.J. Patey, R. Büchel, S.H. Ng, F. Krumeich, S.E. Pratsinis, P. Novák, Flame cosynthesis of LiMn₂O₄ and carbon nanocomposites for high power batteries, J. Power Sources 189 (2009) 149–154, https://doi.org/10.1016/j. ipoweour 2008 10.002
- [64] L. Martínez, R. Andrade, E.G. Birgin, J.M. Martínez, PACKMOL: a package for building initial configurations for molecular dynamics simulations, 2009 (accessed 13)
- [65] J.M. Martínez, L. Martínez, Packing optimization for automated generation of complex system's initial configurations for molecular dynamics and docking, J. Comput. Chem. 24 (2003) 819–825, https://doi.org/10.1002/jcc.10216.
- [66] P. Majerič, R. Rudolf, Advances in Ultrasonic Spray Pyrolysis Processing of Noble Metal Nanoparticles-Review, Materials (Basel, Switzerland) 13 (2020), https://doi. org/10.3390/ma13163485.
- [67] N. Jüngst, I. Skenderović, B.A. Südholt, G.J. Smallwood, F.E. Kruis, S.A. Kaiser, High-speed imaging and statistics of puffing and micro-exploding droplets in sprayflame synthesis, Appl. Energy Combust. Sci. 15 (2023) 100167, https://doi.org/ 10.1016/j.jaecs.2023.100167.
- [68] R. He, K.H. Luo, Atomistic insights into role of urea additive in lithium nanoparticles formation, Chem. Eng. J. 497 (2024) 154822, https://doi.org/ 10.1016/j.cej.2024.154822.
- [69] R. He, K.H. Luo, Mechanisms of microexplosion-accelerated pyrolysis and oxidation of lithium-containing droplets: an atomistic perspective, Nanoscale 16 (2024) 16119–16126, https://doi.org/10.1039/D4NR00592A.
- [70] A.J. Gröhn, S.E. Pratsinis, K. Wegner, Fluid-particle dynamics during combustion spray aerosol synthesis of ZrO₂, Chem. Eng. J. 191 (2012) 491–502, https://doi. org/10.1016/j.cei.2012.02.093.
- [71] A.J. Gröhn, S.E. Pratsinis, A. Sánchez-Ferrer, R. Mezzenga, K. Wegner, Scale-up of Nanoparticle Synthesis by Flame Spray Pyrolysis: The High-Temperature Particle Residence Time, Ind. Eng. Chem. Res. 53 (2014) 10734–10742, https://doi.org/ 10.1016/scp.1209.
- [72] A. Stukowski, Visualization and analysis of atomistic simulation data with OVITO-the Open Visualization Tool, Model. Simul. Mater. Sci. Eng. 18 (2009) 015012, https://doi.org/10.1088/0965-0393/18/1/015012.
- [73] M. Döntgen, M.D. Przybylski Freund, L.C. Kröger, W.A. Kopp, A.E. Ismail, K. Leonhard, Automated Discovery of Reaction Pathways, Rate Constants, and Transition States Using Reactive Molecular Dynamics Simulations, J. Chem. Theory Comput. 11 (2015) 2517–2524, https://doi.org/10.1021/acs.jctc.5b00201.
- [74] OriginPro, Version 2024b. OriginLab Corporation, Northampton, MA, USA.
- [75] Y. Ji, J. Zheng, D. Qin, Y. Li, Y. Gao, M. Yao, X. Chen, G. Li, T. An, R. Zhang, OH-Initiated Oxidation of Acetylacetone: Implications for Ozone and Secondary

- Organic Aerosol Formation, Environ. Sci. Technol. 52 (2018) 11169–11177, https://doi.org/10.1021/acs.est.8b03972.
- [76] Y. Madhavan, K. Ponnammal, K. Ramachandran, T.M. Haridasan, Mean square displacement (MSD) of neighbours around a vacancy in some zinc based tellurides, Phys. Status Solidi B 162 (1990) 119–123, https://doi.org/10.1002/ pssb.2221620108.
- [77] S.S. Sazhin, T. Bar-Kohany, Z. Nissar, D. Antonov, P.A. Strizhak, O.D. Rybdylova, A new approach to modelling micro-explosions in composite droplets, Int. J. Heat Mass Transf. 161 (2020) 120238, https://doi.org/10.1016/j. iiheatmasstransfer.2020.120238.
- [78] H.z. Sheng, L. Chen, C.k. Wu, The droplet group micro-explosions in W/O diesel fuel emulsion sprays, J SAE Transactions (1995) 1534–1542.
- [79] J.D. Groeneveld, S. Pokhrel, L. M\u00e4dler, Flame emission spectroscopy of single droplet micro explosions, J Nanoscale Horizons 9 (2024) 956–967, https://doi. org/10.1039/D3NH00558E.
- [80] R.A. Lalancette, D. Syzdek, J. Grebowicz, E. Arslan, I. Bernal, The thermal decomposition and analyses of metal tris-acetylacetonates, J. Therm. Anal. Calorim. 135 (2019) 3463–3470, https://doi.org/10.1007/s10973-018-7598-8.
- [81] L. Buss, D. Noriler, U. Fritsching, Impact of reaction chamber geometry on the particle-residence-time in flame spray process, FTaC 105 (2020) 1055–1086, https://doi.org/10.1007/s10494-020-00187-1.
- [82] C. Dimitriou, P. Psathas, M. Solakidou, Y. Deligiannakis, Advanced flame spray pyrolysis (FSP) technologies for engineering multifunctional nanostructures and nanodevices, Nanomaterials-Basel 13 (2023) 3006, https://doi.org/10.3390/ page 12323006
- [83] M. Lempart, A. Derkowski, K. Luberda-Durnaé, M. Skiba, A. Błachowski, Dehydrogenation and dehydroxylation as drivers of the thermal decomposition of Fe-chlorites, Am Min 103 (2018) 1837–1850, https://doi.org/10.2138/am-2018-6541
- [84] M. Augustin, D. Fenske, I. Bardenhagen, A. Westphal, M. Knipper, T. Plaggenborg, J. Kolny-Olesiak, J. Parisi, Manganese oxide phases and morphologies: A study on calcination temperature and atmospheric dependence, Beilstein J. Nanotechnol. 6 (2015) 47–59, https://doi.org/10.3762/bjnano.6.6.
- [85] K.W. Chair, I. Leonhard, K. Papusha, M. Schmalz, F.F. Solbach, ChemTraYzer (version 3.0.0b3).
- [86] D.Y. Kim, L. Yang, N. Li, L. Tang, K. Amine, H.-K. Mao, Oxygen-Rich Lithium Oxide Phases Formed at High Pressure for Potential Lithium–Air Battery Electrode, Adv. Sci. 4 (2017) 1600453, https://doi.org/10.1002/advs.201600453.
- [87] A. Ogata, T. Shimizu, S. Komaba, Crystallization of LiMn₂O₄ observed with high temperature X-ray diffraction, J. Power Sources 174 (2007) 756–760, https://doi. org/10.1016/i.jpowsour.2007.06.150.
- [88] R. Ledwaba, M. Matshaba, P. Ngoepe, Molecular dynamics simulations of spinels: LiMn₂O₄ and Li₄Mn₅O₁₂ at high temperatures, IOP Conf. Ser.: Mater. Sci. Eng. 80 (2015) 012024, https://doi.org/10.1088/1757-899X/80/1/012024.
- [89] P. Chand, V. Bansal, S. Ial, A. Joshi, S. Khera, A. Kumar, Effect of annealing temperatures on optical and electrochemical behavior of spinel LiMn₂O₄ as cathode materials for lithium-ion batteries applications, J. Mater. Sci.: Mater. Electron. 32 (2021) 1–12. https://doi.org/10.1007/s10854-021-05380-0.
- [90] A. Othman, H.J. Kim, R. Trivedi, T. Kulasingam, J. Seo, Understanding and mitigating temperature-induced agglomeration in silica-based chemical mechanical planarization (CMP) slurry storage, COLL SURF A 691 (2024) 133802, https://doi.org/10.1016/j.colsurfa.2024.133802.
- [91] R. Mueller, R. Jossen, H.K. Kammler, S.E. Pratsinis, M.K. Akhtar, Growth of zirconia particles made by flame spray pyrolysis, AIChE J. 50 (2004) 3085–3094, https://doi.org/10.1002/aic.10272.
- [92] N. Saadatkhah, S. Aghamiri, M.R. Talaie, G.S. Patience, Flame-assisted spray pyrolysis of lithium and manganese precursors to polycrystalline LiMn₂O₄, CJCE 97 (2019) 2299–2308, https://doi.org/10.1002/cjce.23302.